ACOUSTIC EMISSION AND DAMAGE EVOLUTION IN STEEL FIBER-REINFORCED CONCRETE BEAMS UNDER CYCLIC LOADING

Hernán XARGAY [1,2], Marianela RIPANI [2], Paula FOLINO [2], Nicolás NÚÑEZ [1], Antonio CAGGIANO [2,3,*]
[1] Comisión Nacional de Energía Atómica (CNEA), Departamento ICES, Buenos Aires, Argentina
[2] Universidad de Buenos Aires, Facultad de Ingeniería, INTECIN (UBA-CONICET), Buenos Aires, Argentina
[3] Institut für Werkstoffe im Bauwesen, Technische Universität Darmstadt, Darmstadt, Germany

*Corresponding author: acaggiano@fi.uba.ar

ABSTRACT: In this work, the Acoustic Emissions (AEs), detected in real-scale Reinforced Concrete (RC) beams which have been tested under four-point bending, are investigated and correlated with their structural responses and damage evolutions. Two different reinforcing bar arrangements, with or without shear stirrups, were designed in order to obtain bending or shear failure modes, respectively. Moreover, some of the beams were casted with the addition of steel fibers in the concrete mixture. A loading procedure characterized by several cycles of increasing amplitude up to failure was implemented. Beams failure behaviors and the aptitude of four AE-based indices to assess their damage level, are presented and compared. Moreover, some relevant variables possibly affecting the indices performance are analyzed. The steel fibers enhanced shear strength by restricting the development of inclined cracks in the beam without stirrups. Finally, it can be figured out that AE indices showed a quite good correlation with cracking initiation and progression. Therefore, they proved to be competent for both monitoring the RC beams loading response and detecting eventual local damages, even for fiber-reinforced concrete members.

KEYWORDS: Acoustic Emission, Damage Assessment, SFRC, Cyclic loading, AE-based indices.

1 INTRODUCTION

In the field of structural engineering, there is a growing demand to develop Non-Destructive Testing techniques (NDTs) capable of monitoring and evaluating the health condition of existing Reinforced Concrete (RC) elements and structures [1]. In the last decades, plenty of NDTs have been conceived or applied to buildings and structures and they are continually improved. Some of them are: the parallel seismic method [2], the impulse response method [3], the impact-echo method [4], the ultrasonic tomography [5], the ground penetrating radar [6] and the impedance tomography [7]. Among these NDTs, a great interest is currently placed on damage qualification criteria based on Acoustic Emission (AE) monitoring [8], where it is worth mentioning the multi-technique approaches, which combine AE with dynamic identification and/or digital image correlation techniques [9-10-11].

It is a well-known fact that AEs are transient elastic waves that propagate within the range of ultrasonic frequencies. They are generated due to the rapid release of energy inside of a given material under certain conditions [12]. Thus, AE-based NDT consists in detecting, processing and analyzing AE waves generated from localized sources when a material or structure is conveniently stressed at different levels. This allows the structural monitoring in a passive and non-invasive manner [13]. So far, AE monitoring has been studied and implemented in laboratory tests and field applications, intended at scrutinizing the structural health status of RC elements [14, 15, 16, 17, 18, 19]. Consequently, some indices have been proposed based on AE signal parameters [20, 21, 22, 23], which are conceptually linked to the occurrence of the characteristic phenomenon

generally referred to as “Kaiser effect”. Particularly, Kaiser effect is related to those materials that behave elastically during repeated loading cycles [24]. In fact, under loading, unloading and reloading processes, new AE detections will not take place if the highest load, previously reached by the material, has been not overcame [25]. On the other hand, once cracks, damage or plastic strains begin, new AE activity occurs and the Kaiser effect starts to be not fulfilled, thus the ratio between the applied load at which AE starts and the preceding maximum load, takes the name of Felicity Ratio (FR) [26].

With regard to computational simulations, in the current literature it can be found some numerical procedures intended at describing the wave propagations and their coupling with fracture mechanisms in cohesive frictional cracked media. Particularly, some mathematical models attempted to find a correlation between micro-to-macro fracture relationships and acoustic waves in rocks and cementitious composites [27, 28, 29]. Recently, the so-called Time Reverse Modeling (TRM) was proposed as a localization technique for numerically investigating the AE activity due to concrete cracking [30, 31]. On the other hand, Finite Element (FE)-based analyses capable to simulate waves propagation coupled with stress-based simulations are available in commercial software, e.g., COMSOL [32], ANSYS APDL [33] and FEMAP coupled with NX NASTRAN [34]. Nevertheless, the involved complexity of the processes and their couplings are so computationally demanding that these approaches are still in an incipient stage of development. Therefore, so far it is not possible to adequately simulate the AE response and its understanding is mainly sought through experimental studies.

Concerning technical standardization for damage assessment using AE, some standards and recommended practices/guidelines are currently available. In this work, the recent standard ISO 16837 (2019) [35] is taken as a reference. It is concerned with a testing method for damage qualification of RC beams through the use of AE indices. As a matter of fact, it was inspired on the previous recommendations RILEM TC 212-ACD [36] and JSNDI NDIS 2421 [37]. Basically, ISO 16837 proposes a damage classification chart defined by two AE indices: (i) the Load Ratio (LR) and (ii) the Calm Ratio (CR). The first one is, in fact, the above-mentioned FR and represents a critical parameter for AE monitoring that decreases with damage accumulation. The second one, hereafter namely CR, deals with the cumulative AE activity under the unloading phase to the total cumulative AE activity during the entire cycle. Consequently, this method must be applied to AE activity obtained from incremental and cyclic loading tests. However, it is worth mentioning that one of the main shortcomings in AE-based damage assessments is that it is still not feasible to determine absolute threshold indices values or their expected variation ranges. This is due to the influence of structure/sample sizes, test conditions and employed instrument types on the method performance. At the same time, the lack of available extensive experimental results constitutes a further limitation. To overcome this deficiency, more experimental data are required in order to validate these testing procedures and their acceptance criteria for assessing RC structures. Furthermore, researches regarding new concretes in order to extend their field of application, such as fiber-reinforced concrete [38, 39] and high-performance concrete must be performed [40].

An important issue that has not been explained in detail in previous works is how different experimental variables could affect the AE indices results. Sensors location in terms of shear and pure bending span is one of them. Other variables are the reinforcement configurations and amounts (either bars, stirrups or fibers) and their relation to the failure mode. In general, several studies have reported two very different behaviors in terms of AE according to the failure mode [35]. Therefore, this aspect is analyzed here and, as a novelty, the effect of the addition of steel fibers as structural reinforcement is also considered. The reloading cycle in which the indices are calculated is a variable which influence is still not well documented in the literature. It is expected that the AE response changes between the first and subsequent repeated loading cycles due to the possible growth (or not) of cracks. In fact, there are no standardized loading protocols for testing RC members specifically with the AE method.

This research aims at studying the structural response and AE evolution of real scale RC beams subjected to cyclic loading tests. One of the main goals of this work is to investigate the possible correlations between AE indices (i.e., Load, Calm, Cumulative Signal Strength and Relaxation ratios) and relevant damage levels of RC members. The influence of the aforementioned variables on the experimental results is also examined and discussed.

After the above introductive section, the materials and methods of the experimental program are reported in Section 2. Next, the obtained structural results from the tested beams are shortly described in Section 3. In Section 4, a broad discussion on damage evaluation based on the available AE indices is performed. Concluding remarks of this research and future developments are addressed in Section 5.

2 EXPERIMENTAL PROGRAM

The experimental tests presented in this paper were carried out at the Laboratory of Materials and Structures of the University of Buenos Aires (UBA) in collaboration with the Argentinean National Commission of Atomic Energy (CNEA). Real-scale RC beams with different steel reinforcement layouts were evaluated. In this section, materials, methods and the experimental campaign as whole have been described.

2.1 Materials

The plain concrete mixture was planned in order to obtain a target 28 days mean compressive strength of 30 MPa, measured on cylindrical specimens, and a slump value of 120 mm. In this regard, a water-to-cement ratio of 0.49 (w/c) was adopted. The basic constituents used for the mixture were: Portland cement with similar features to CEM 42.5R, a graduated combination of natural river sand and crushed stone sand as fine aggregates, coarse crushed stone with maximum size of 20 mm, potable water and normal-range plasticizer. Further details about mixture composition are given in Table 1. It is worthwhile to mention that the mechanical characterization of this concrete was performed in a previous work by the authors [41]. For the sake of brevity, only three relevant properties, i.e., compressive, splitting tensile and three-point bending (TPB) peak strengths are listed in Table 2.

Regarding the steel fibers, cold drawn steel wire fibers type Wirand FF3® were selected (see Figure 1). These fibers are hooked-ended, with diameter (d_f) equal to 0.75 mm and nominal length (L_f) equal to 50 mm, leading to an aspect ratio (L_f/d_f) of 67. The main mechanical properties reported by the manufacturer are: tensile strength of 1100 MPa, ultimate strain of 4% and Young's Modulus of 200 GPa. The fibers were incorporated into the concrete mixture as an additional component in a volume fraction of 0.50% (40 kg/m^3).

Table 1: Concrete mixture composition.

Constituent material	**Proportion** [kg/m^3]
Cement	340
Siliceous river sand	560
Fine crushed granitic aggregate	240
Coarse crushed granitic aggregate	1060
Water	166
Plasticizer	1.36
Steel fibers	40

Table 2: Concrete mechanical properties [41].

Concrete type	**Plain concrete**	**Fiber-reinforced concrete**
Compressive strength [MPa]	32.31	35.35

Splitting tensile strength [MPa]	4.34	6.70
TPB peak strength [MPa]	3.25	4.47

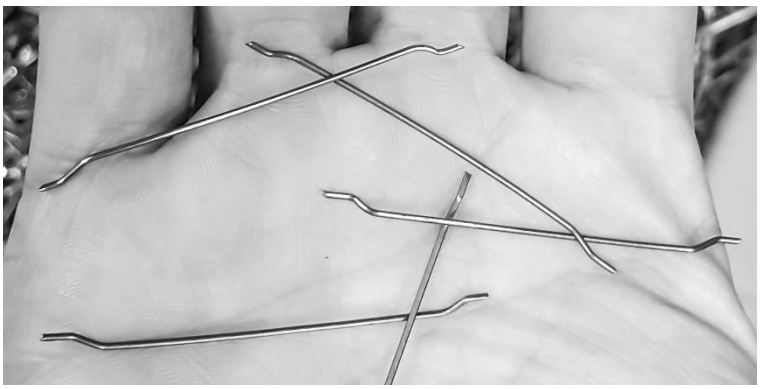

Figure 1. Steel fibers Wirand FF3® type.

Deformed steel bars with diameters of 6 and 12 mm were used as shear and flexural reinforcements, respectively. Their most important mechanical properties were: nominal yield stress of 420 MPa (defined at 0.2% offset strain), tensile strength of 500 MPa, ultimate strain of 12% and Young's Modulus of 200 GPa.

2.2 Reinforced Concrete beams

Four full-scale RC beams were casted into polymer formworks, properly vibrated and cured for 3 months under laboratory-controlled conditions before testing. The beams dimensions were: width (b_w) of 120 mm, height (h) of 300 mm and total length of 2400 mm. Two reinforcing bar layouts were designed in order to obtain different failure modes. More specifically, two of the beams, hereafter referred to as "B", were devised to have a tension controlled bending failure, meanwhile the remaining two beams, referred to as "S", were expected to have a shear failure. Table 3 gives overview information about the considered four real-scale beams and their adopted reinforcements. Particularly, the so-called B group had 2ϕ12 bars as tension reinforcement, 2ϕ6 bars as compression reinforcement and ϕ6 closed stirrups 150 mm spaced, while the S group had 4ϕ12 reinforcing bars as tension reinforcement, 2ϕ6 bars as compression one and without stirrups. The tensile reinforcement ratio (ρ), computed as the tensile steel area (A_s) to the effective cross of concrete ($b_w \times d$) was 0.70% for the B group and 1.50% for the S one. Furthermore, both B and S samples were subdivided into plain concrete and fiber-reinforced concrete (FRC) specimens, being BP and SP, the beams poured with plain concrete while BF and SF the ones made with FRC. Bar configurations are depicted in Figure 2. It is worth highlighting that BP beam was under-reinforced for bending and fully reinforced against shear failure, whereas beam SP had double reinforcement for bending than the former but non-reinforced against shear failure. In the case of SF the ultimate shear strength should be mainly provided by the action of steel fibers.

Table 3: Reinforcements adopted in the analyzed beams.

Beam	**Steel reinforcement**		**Steel fibers**	
	bars	**stirrups**	**volume fraction** [%]	**in weight** [kg/m^3]
BP	2ϕ12 (tension) 2ϕ6 bars (compression)	ϕ6 closed/150 mm	-	-
BF			0.50	40
SP	4ϕ12 (tension) 2ϕ6 bars (compression)	-	-	-
SF			0.50	40

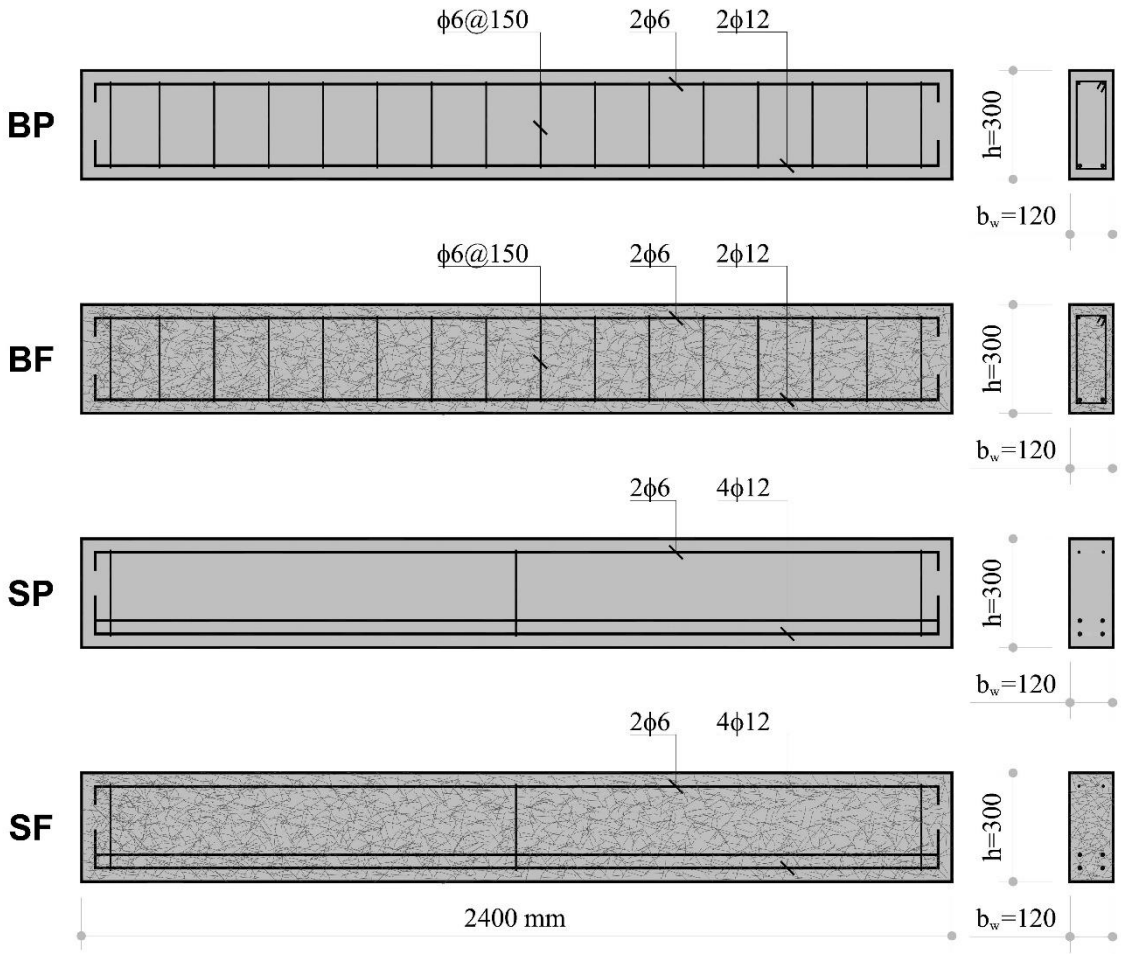

Figure 2. Geometry and reinforcement configurations of B and S beams.

2.3 Methods

In the following section, the mechanical testing setup, details of the cyclic loading procedure as well as the AE monitoring configuration are described.

2.3.1 Test setup

Mechanical evaluation consisted of Four-Point Bending (FPB) tests on real-scale simply supported beams. Loads were applied on the third points of the beam by means of two hydraulically actuated and coupled jacks with a maximum capacity of 200 kN each one. The tests were executed under load control with a target loading/unloading rate of 150±15 N/s. The distance between beam supports was 2100 mm.

Regarding the structural response measuring, compressive strain, crack width and deflection were continuously monitored through Linear Variable Differential Transformer (LVDT) sensors, attached at the mid-span section. In addition, cracks width along the beam span were also measured by using an USB microscope (with ×400 magnification) during loading holds. By last, a load cell was placed under a jack to continuously record the applied load. Figure 3 (a) shows the view of the loading frame and general test arrangement, while Figure 3 (b) details the beam setup and instrumentation above described.

(a)

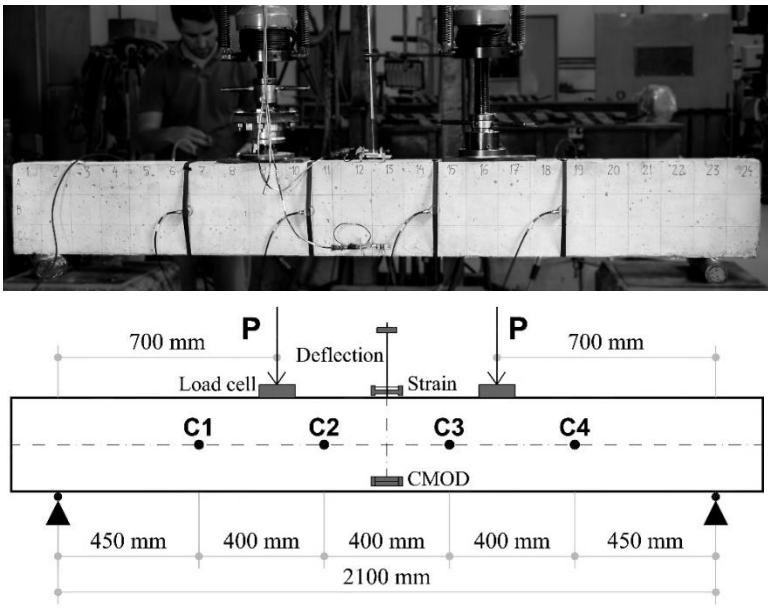

(b)

Figure 3. Test arrangement: (a) loading frame and (b) beam setup and instrumentation.

2.3.2 Cyclic loading procedure

The beams were subjected to a cyclic loading procedure with at least five load incremental levels. At each load level a fixed increment of 8.8 kN was added. Additionally, two loading/unloading cycles as recommend by [42] were carried out at each load level, named cycles A and B. Maximum load at B cycles was maintained for 3 minutes in order to stabilize the structural response and to measure the cracks widths and their path growths. In all cycles the unloading phase was finished at a minimum load of 3 kN, in order to keep the test jacks engaged. As example, Figure 4 shows the loading scheme for SF beam.

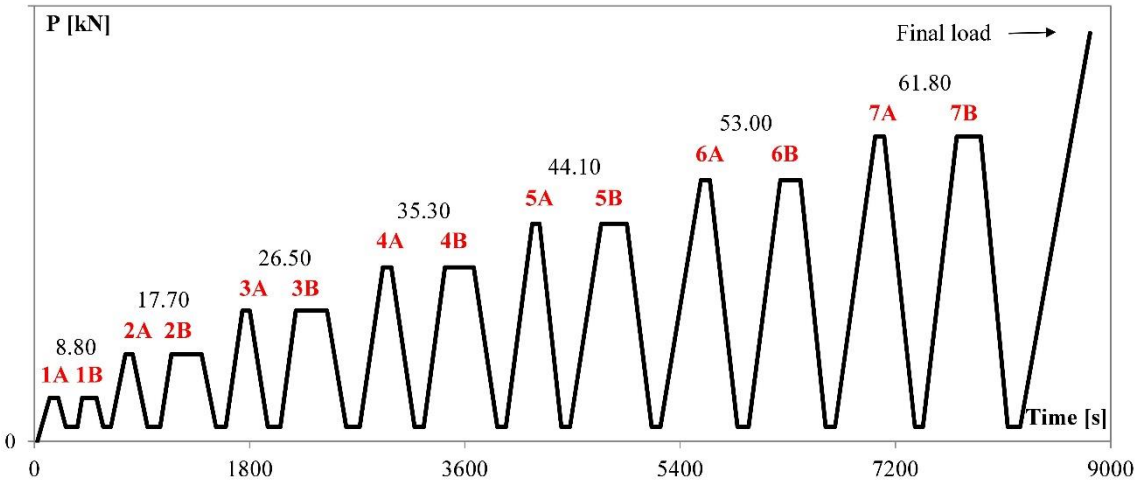

Figure 4. Cyclic loading procedure and maximum load levels values applied by each jack in SF beam.

As mentioned before, the loading protocol was executed until reaching the beam global failure, i.e., when concrete fracture was observed or a continually loss of load carrying capacity was registered. As an exception, in SF beam the last load level was at 61.8 kN and after that the beam was monotonically loaded up to failure for safety reasons. Total duration of each test ranged from 1.5 to 3 hours. It must be highlighted that there are no available standardized loading protocols or guidelines for testing RC beams together with AE-based methods/monitoring.

2.3.3 AE monitoring setup

AE signals were continuously recorded throughout the whole mechanical test. To this end, two PAC PCI-2 AE acquisition boards were employed and four sensors (R15-I model with 150 kHz resonant peak frequency) were mounted on the beams front face. These sensors were symmetrically placed at middle height of the specimens and horizontally spaced 400 mm. Well-known is the fact that the FPB scheme leads to a theoretical pure bending stress state -i.e. without shear forces- between the two loading contact points, where uniform and maximum bending moment takes place. Therefore, channels C2 and C3 where deliberately located at the central bending span, meanwhile channels C1 and C4 were opportunely positioned at the shear spans. The resonant sensors were chosen for two key reasons. On the one hand, the distances between the sensors were small and it was desired to reduce signals mixing and rebounds between different channels. On the other hand, resonant sensors supplied an adequate balance between sensitivity and attenuation reducing low frequency background noise. In order to couple the sensors to the concrete, solid vaseline was used. Also, the sensors were fixed and secured to the beam by means of plastic tape. Very thin low-friction PTFE sheets were placed between specimens and steel supports in order to reduce possible frictions and related noises. Before tests started, coupling and attenuation of signals were checked at different surfaces points creating artificial sources obtained by breaking pencil leads. The system was setup with a measurement threshold of 40 dB, a band-pass filter of 20-400 kHz and a sampling frequency of 2 MHz. In order to remove spurious hits without physical meaning, AE raw data were pre-filtered by magnitude of AE parameters. Finally, emission sources were verified with a zone location criterion based on time of arrival to AE channels.

2.3.4 AE damage indices

The AE analysis is based on the following four AE damage indices: Load Ratio (LR), Calm Ratio (CR), Cumulative Signal Strength Ratio (CSSR) and Relaxation Ratio (RR). These indices are defined according to Eqs. (1) to (4) as follows:

$$\text{Load Ratio} = \frac{\text{load at the onset of AE activity during reloading}}{\text{previous maximum load}} \quad (1)$$

$$\text{Calm Ratio} = \frac{\text{Cumulative Signal Strength during unloading}}{\text{Cumulative Signal Strength during the whole cycle}} \quad (2)$$

$$\text{CSS Ratio} = \frac{\text{Cumulative Signal Strength during reloading}}{\text{Cumulative Signal Strength during previous reloading}} \quad (3)$$

$$\text{Relaxation Ratio} = \frac{\text{Average Signal Strength during unloading}}{\text{Average Signal Strength during previous loading}} \quad (4)$$

In Eq. (2), AE Signal Strength (i.e., the measured area below the rectified AE signal) was chosen as the main input parameter for CR instead of the traditional number of hits. This adaptation was made because Signal Strength implicitly involves to the amplitude and the duration of the hit, weighting the actual magnitude of hits sourced from further away. Also, in Eq. (4), AE Signal Strength was adopted as replacement of AE Energy used in the original proposal [21].

3 RESULTS AND DISCUSSION ON STRUCTURAL BEHAVIOR

In this section, visual examination of the cracking pattern evolution and structural measurements on beams loading response are presented and outlined. Based on that evidence, their failure behaviors are compared and the fibers effect is also assessed.

3.1. Beams – B group

During the progress of the Load Level 1 (LL1: 8.8 kN), as predicted by calculus, no cracks were revealed. First cracks occurred nearly to 10 kN for both samples (BP and BF, respectively), i.e., during the loading to LL2 (17.7 kN). They were located in the vicinity of central span and developed a considerable height, reaching until 50%×h (beams height). At the end of LL2, a little less crack development on BF compared with BP was observed. At LL3 (26.5 kN), few new cracks appeared at central span and most of them grew up until 60%×h. Also, first slightly inclined shear cracks appeared. At that point, both beams had similar cracking patterns. During LL4 stage (35.3 kN), new shear cracks became evident and the flexural ones propagated a little more upward till 65%×h. At LL5 (44.1 kN) new inclined cracks were discovered and were larger and closer to supports at BP than BF. The existing flexural cracks became wider and almost without change in height. This phase is referred as the stabilized cracking stage. Overpassing LL5 maximum load, both beams reached a yielding plateau, so it was not practically possible to continue increasing the load and to perform another load level. Tests were stopped when the failure became localized at central span at some predominant cracks and the concrete top zone started to crush. The maximum registered load (P_{max}) for BP was 49.1 kN and for BF was 50.5 kN. Cracking configurations of B beams are shown in Figure 5 (a) and (b) and their final aspects are presented in Figure 6 (a) and (b).

In summary, B samples showed a very ductile failure process. It was supposed that fibers could contribute providing tensile strength for BF and, hence, lowering the neutral axis. However, as shown in Figure 7 (a), stiffness, maximum deflection and ultimate loads were quite similar for both BP and BF. Therefore, the steel fibers addition in a volume fraction of 0.50% did not substantially modify the overall mechanical performance of BF beam. It must be highlighted that at the end of LL5 crack heights were practically the same for both, showing that the difference in neutral axis position and curvature were not significant. Nevertheless, it could be appreciated a slight delay in the cracks progress at LL2 for BF. Also, shear cracks next to supports were more developed at BP than BF. Moreover, it can be noted that BF presented a few more and short flexural cracks in comparison with BP at their final state. These facts can be attributed to the fibers bridging mechanisms, which causes the arrest of cracks propagation and a redistribution of stresses.

3.2. Beams – S group

S beams had a strongly differentiated failure. Although a global shear-mode failure could be expected for this layout due to the lack of stirrups, this brittle failure type only occurred for the SP sample, as detailed below.

During LL1 both beams remained uncracked. Again, first cracks occurred nearly to 10 kN, when coursing LL2. They were also located in the vicinity of central span, zone of maximum bending moment, but developed a shorter height than those in B samples (Section 3.1), around 35%×h for SP. Similarly, to B beams, at the end of LL2 less amount and even shorter height growth was noted in the SF cracks in comparison with SP. At LL3 stage, only few new flexural cracks appeared at SP and some grew in height until 50%×h. In the case of SF, several new flexural cracks became visible at this stage but with reduced growth and limited to 40%×h. At LL4, the existing cracks propagated a little more upward, surpassing 60%×h for SP and reaching 50%×h for SF. First shear cracks became visible at SP in this stage. In LL5, S beams clearly changed their structural behavior showing a bifurcation. For SP, new inclined cracks propagated upward until 70%×h, anticipating a forthcoming shear failure. First inclined shear cracks restricted to 50%×h appeared at SF. Just when performing the second load hold at LL6, SP specimen showed a prematurely failure without reaching a yielding plateau: one mayor inclined shear crack suddenly grew up in an angle of 30 degrees reaching to the load contact point. On the other hand, SF overpassed LL6 showing few remarkable changes: the existing cracks evolved wider and almost without change in height (between 50-65%×h) and only a few new shear cracks appeared. At LL7, few new flexural and shear cracks became evident and, then, SF started the stabilized cracking stage. After LL7 cycling, SF was loaded monotonically until reached a yielding stage. The failure of SF beam was due to a localized flexural crack at central span that generated the concrete top zone started to crush. At the same moment, it was also noticed that wide inclined shear cracks between the jack and the support were very close of producing the beam failure. The maximum registered load P_{max} was 53.6 kN for SP and 82.8 kN for SF. Cracking patterns of S beams are depicted in Figure 5 (c) and (d) and their failure views are revealed in Figure 6 (c) and (d).

Summarizing, after first cracks occurred, the subsequent decrease in stiffness was approximately the same for both SP and SF (Figure 7 a). Then, their structural behavior were similar, with only a slight cracking evolution delay in SF due to fibers, until first shear cracks became evident. The addition of fibers clearly influenced the mechanical behavior of SF beam acting as an effective shear reinforcement. Moreover, the bridging effect of fibers on the inclined shear cracks gave post-cracking tensile resistance and led to a yielding stage, developing more cracks than SP but shorter and, in some cases, discontinuous. Even shear cracks shifted their inclination angles from approximately 30 to 40 degrees. The fact that inclined shear cracks had a considerable development at SF failure, pointed out that the fibers addition in a volume fraction of 0.50% were close to the limit of failure modes change for this particular reinforcement configuration.

Figure 7 (b) shows comparatively the load versus crack width response for all the beams. Only the maximum crack width at mid-span of the second cycle (B) of each load level are plotted for simplicity. BP has the widest cracks, while the BF curve displays an offset that reveals the fibers effect on bridging cracks opening. Lastly, SP and SF exhibit a similar trend with thinner cracks, showing the predominant influence of the higher reinforcement ratio. Table 4 summarizes the evolution of the different structural measurements at mid-span obtained for all the considered beams.

In comparison, under-reinforced B beams presented less, higher and more spaced cracks than S beams. For each load level, crack widths were wider for B specimens than S because of the higher reinforcement ratio. Also, it was verified that steel fibers addition in a volume fraction of 0.50% was more effective for improving shear strength and giving more ductile failure than for contributing in flexural strength. At low stress levels, fibers seem to partially restrict the cracking development.

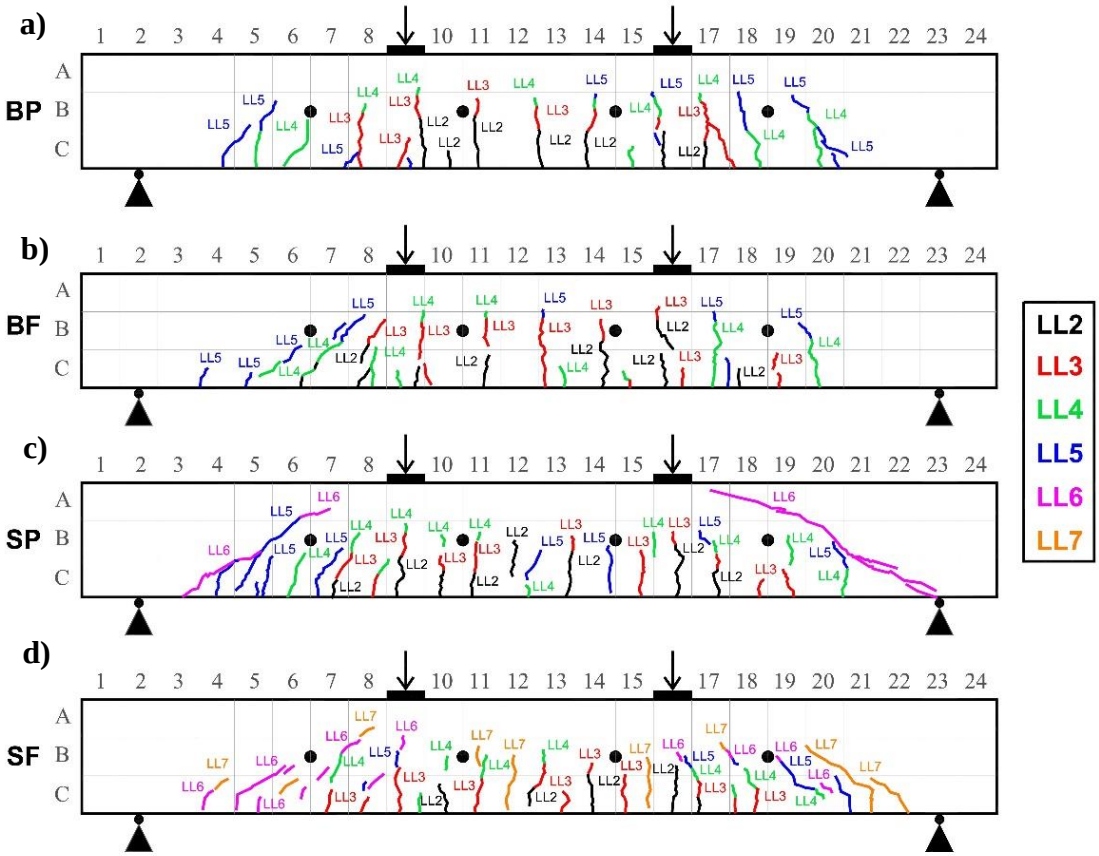

Figure 5. Cracking patterns diagrams: (a) BP, (b) BF, (c) SP and (d) SF.

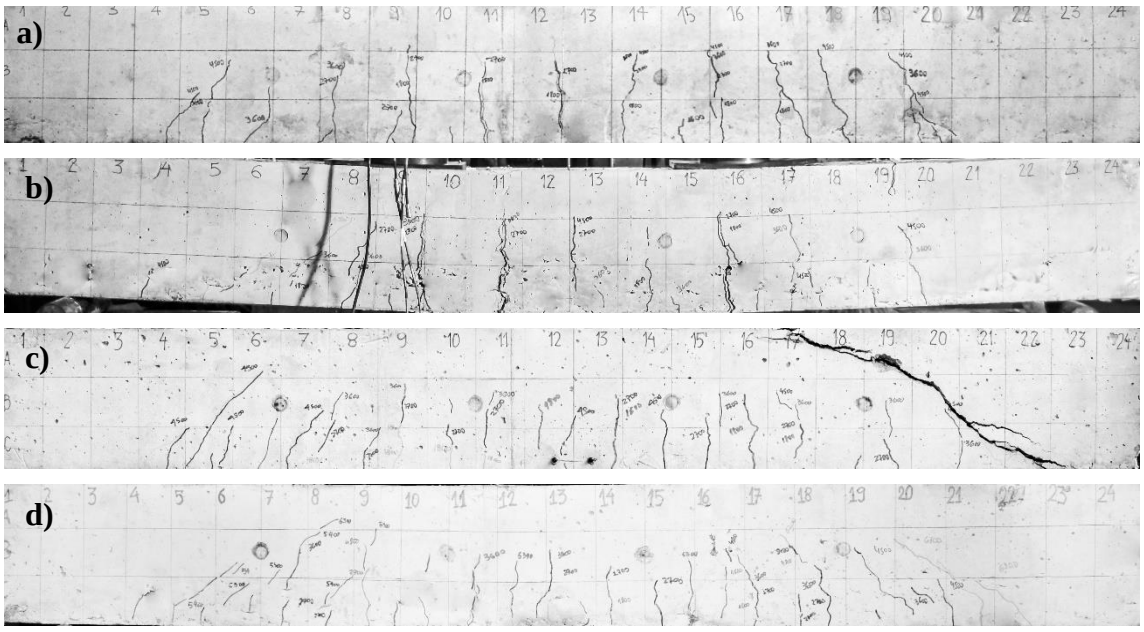

Figure 6. Failure modes: (a) BP, (b) BF, (c) SP and (d) SF.

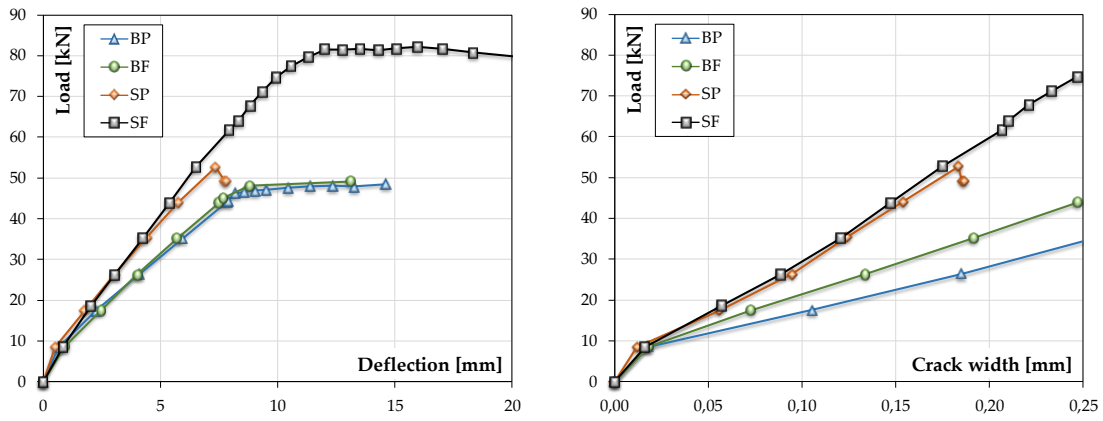

(a) (b)

Figure 7. Beams structural response: (a) Load vs. Deflection and (b) Load vs. Crack width. For simplicity, only the maximum deflection and crack width at mid-span of B cycle is plotted for each load level.

Table 4**:** Structural measurements.

Load Level	1	2	3	4	5	6	7
Load [kN]	8.8	17.7	26.5	35.3	44.1	53.0	61.8
	BP (P_{max}=49,1 kN)						
P/P_{max} (%)	18%	36%	54%	72%	90%	---	---
Crack width [mm]	0.018	0.105	0.185	0.256	0.326	---	---
Deflection [mm]	0.650	2.270	4.090	5.930	7.830	---	---
	BF (P_{max}=50,5 kN)						
P/P_{max} (%)	17%	35%	52%	70%	87%	---	---
Crack width [mm]	0.018	0.073	0.134	0.191	0.247	---	---
Deflection [mm]	0.920	2.460	4.020	5.700	7.490	---	---
	SP (P_{max}=53,6 kN)						
P/P_{max} (%)	16%	33%	49%	66%	82%	99%	---
Crack width [mm]	0.012	0.056	0.095	0.124	0.154	0.180	---
Deflection [mm]	0.500	1.770	3.040	4.390	5.770	7.360	---
	SF (P_{max}=82,8 kN)						
P/P_{max} (%)	11%	21%	32%	43%	53%	64%	75%
Crack width [mm]	0.016	0.057	0.088	0.121	0.147	0.170	0.210
Deflection [mm]	0.840	2.030	3.040	4.230	5.390	6.510	7.920

4 RESULTS AND DISCUSSION ON ACOUSTIC EMISSION INDICES

In this section, the results of the aforementioned AE-based indices are analyzed. Initially, each index is presented separately and duly examined in terms of cracking and damage evolutions. At the end, the charts suggested by the ISO 16837 standard [35] are depicted and discussed.

It is worth to remark that it has been preferred to study the indices in relation to the level of maximum load (P/P_{max}) instead of the current load (P) or load level (LL), as normally done in other works in the literature. This approach offers several advantages and presents quite good results. Firstly, by using different reinforcement configurations and amounts, individual values of P_{max} are not directly comparable, i.e., the failure processes are more adequately described in

relative (dimensionless) terms to their ultimate loads. Therefore, it allows to compare the different cases in the same scale. Also, in this way it permits to abstract the analysis from the particular loading scheme and beams geometry. Lastly, it is of great interest to correlate AE indices with the damage level (P/P_{max} ratio denotes a kind of damage parameter) since it would be extremely useful if AE provides an early warning of the failure proximity for its practical application.

In the following, the influence of experimental variables (reloading cycle, sensors location, reinforcement configurations and steel fibers addition) on AE results is discussed in detail. To this end, the indices were independently calculated for each AE channel (i.e., C1, C2, C3 and C4) and for each cycle (namely, A and B). Furthermore, as mentioned above, AE channels have been deliberately arranged in both flexural and shear spans to address their particular effects. Likewise, the crack widths are considered since they also constitute a fundamental structural parameter for the serviceability and durability of RC structures.

In this experience, the beams had not been loaded before testing and, therefore, had no previous cracks. Then, the first load level was intentionally established below the initial cracking load, and consequently very limited AE activity was recorded in that stage. For that reason, in some cases the indices calculation gave scattered and meaningless results that are not represented, so, to do not affect the trends. It can be argued that at very low load levels, i.e., below cracking loads, the obtained high values of the CR, CSSR and RR are consequence of very scarce AE activity and not indicative of structural inelastic behavior.

4.1. Load Ratio (LR)

This index is widely used in RC structures and, as stated before, is one of two that are defined by the ISO standard. Its main disadvantage lies in the subjectivity of its definition (i.e., Eq. 1). In fact, an "onset of AE activity" criterion must be established for its calculation and, hence, it could leads to a diverse range of results, from different users. In this work, the slope breakpoint of the cumulative Signal Strength versus time curve was considered to establish this criterion. Nevertheless, it had to be calibrated for each beam and also for each channel, so it was not suitable for calculations in real time when executing the tests. In addition, it is pointed out that for calculation of the LR at the second reloading, named B, the first loading portion of the following LL was used, since until the former maximum load is not exceeded, the last can be considered as a third loading of the preceding LL.

Figure 8 illustrates the LR results separately for each type of beam and loading cycle. In each plot, the AE channels are individually shown and, also, grouped by location in color intensity: those in the flexural span (C2 and C3) are represented in darker tones while those in shear one (C1 and C4) in lighter ones. Thus, the fundamental variables for the analysis can be readily appreciated. In general, LR exhibits a decreasing trend when the load level increases, with values ranging between 1.30 and 0.40. However, as noted before, this range can change according to the adopted criterion and it should be mentioned that in tuning trials, with a stricter criterion, LR showed minimum values as low as 0.20. Therefore, its practical use with fixed limit values seems to be complex to achieve.

As stated in [35], LR values greater than 1.0 are feasible and indicate structural soundness. It was evidenced at the first load levels, before reaching the cracking loads. It can be observed that LR became below 1.0 after initial cracking, occurred during LL2 for all beams, which suggests that the Kaiser effect disappears due to the creation of macrocracks and could not be linked to a certain crack opening displacement value. The measured superficial cracks width, at the end of LL2 cycle B, ranged from 0.05 to 0.10 mm (see Table 4).

The effect of fibers addition is very slight in LR for loads under $50\% \times P_{max}$. It can be appreciated that BF presents higher values of LR in LL2 than BP, supporting the visual observation that comparatively less cracking occurred in BF at this stage. It is also noted that the plain beams have lower values of LR than the fibered ones for load levels higher than $50\% \times P_{max,}$ particularly in the shear spans. This evidences that fibers restrict the shear cracks occurring near the failure. SP

shows lower values of LR than the other beams. It is remarkable that fibers led to a more homogeneous crack pattern in SF, similarly to B beams and differing from SP. Regarding the effect of the reinforcement configuration, there are no evident differences between B and S groups.

It can be also noticed that LR is affected by the repeated loading cycle in which is calculated. If LR is calculated at the first reloading (A), lower values, in the order of 20%, are obtained in comparison with the LR value obtained at the second one (B). However, the tendencies previously described are valid for both repeated loading branches.

In the light of the foregoing, it can be concluded that LR is a damage indicator by itself and is linked to the presence of new cracks, but not necessarily to its width evolution. When new cracks appear LR decreases and then, if no new ones are generated and/or the existing get stabilized, LR tends to be constant. As mentioned in the previous section, the number of flexural cracks tends to stabilize before the shear ones, and the overall cracking pattern does not change considerably at higher loads, but merely widen the existing cracks. It is also reflected in the general tendency of LR, which slope decreases after the initial cracking process, at loads close to 40%×P_{max}. This behavior is more noticeable in the flexural span. In particular, it can be seen that when SP failure was imminent at LL6, LR reached a minimum value of 0.44 at C4 (Figure 8 c). It was there that an inclined shear crack conducted to the failure (see Figure 6 c). Therefore, this supports that LR could act as a damage indicator.

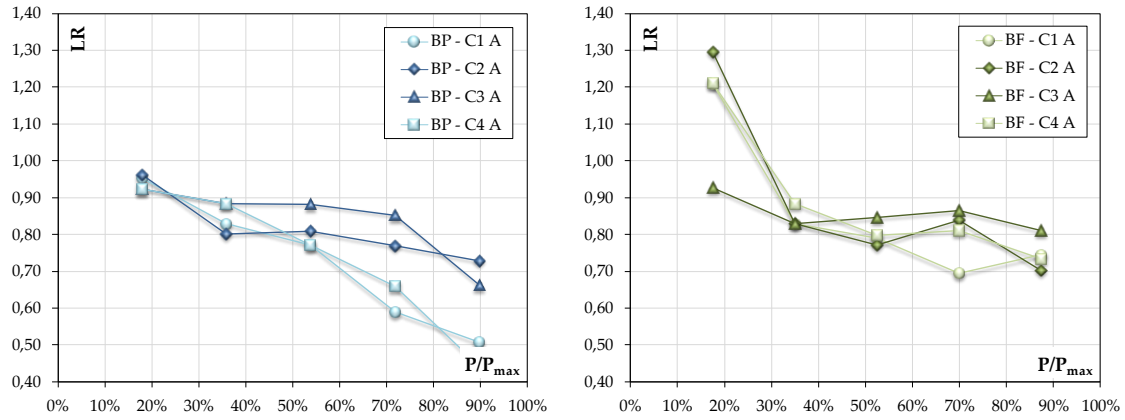

(a) (b)

(c) (d)

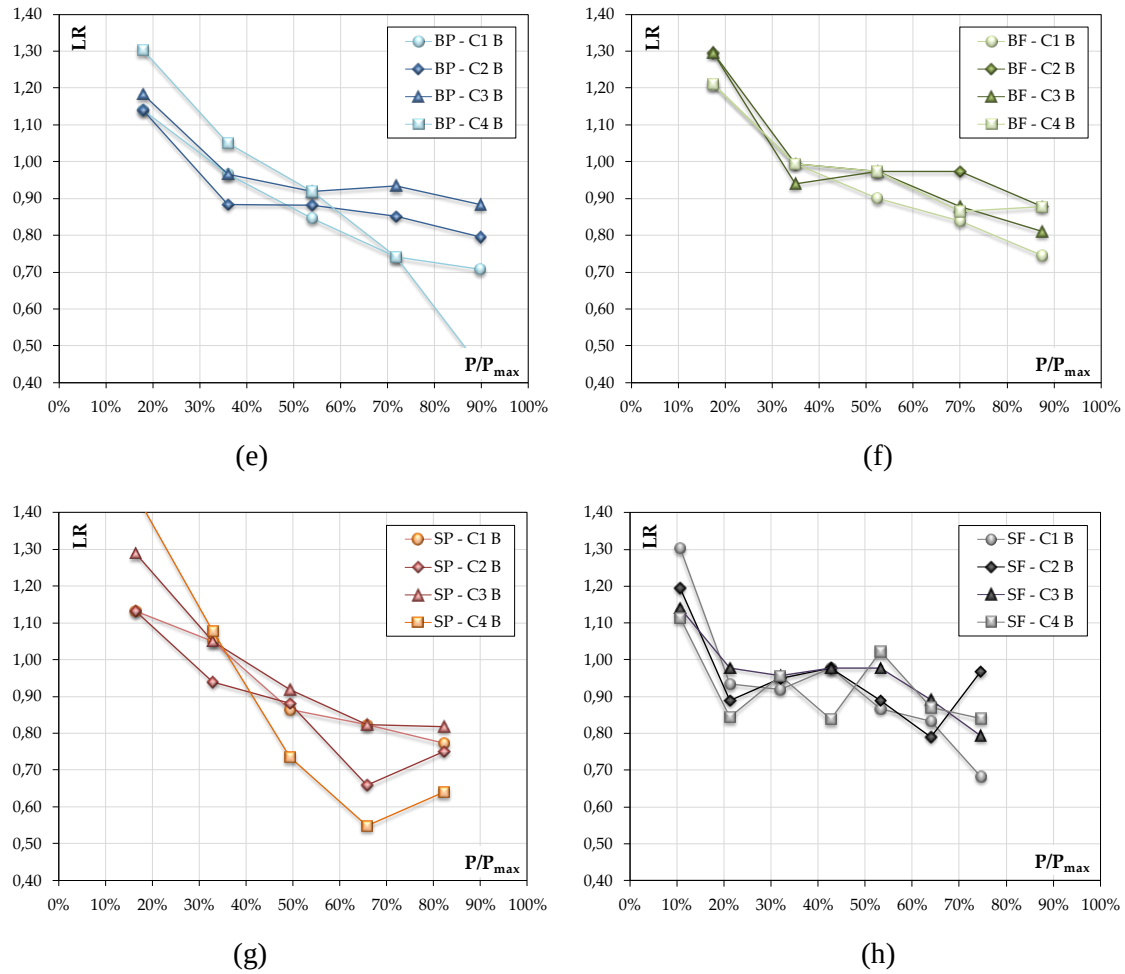

Figure 8. Load Ratio results: (a) BP cycle A, (b) BF cycle A, (c) SP cycle A, (d) SF cycle A, (e) BP cycle B, (f) BF cycle B, (g) SP cycle B and (h) SF cycle B.

4.2. Calm Ratio (CR)

CR substantially differs from LR because explicitly considers the AEs generated during the unloading branch. It is known that the AEs at unloading phase are consequence of complex processes that occur when the closure of existing cracks take place (e.g., friction between surfaces and/or between steel and surrounding concrete). Also, another difference with LR is that CR does not take into account the subsequent reloading phase in its calculation. Therefore, they are considered complementary for damage assessment [35].

This index, as originally proposed by Ohtsu et al. [20], utilizes the AE generated in the entire cycle under analysis as the ratio denominator, and thus, always gives values lower than 1. However, in later works [21, 23], CR has been modified using only the AE of the loading branch up to the maximum load of the considered cycle as the ratio denominator. In consequence, the modified CR may eventually leads to numeric results greater than 1. Both calculation options were evaluated, finding that the original proposal adopted by the ISO standard offers the lesser scattered results. Therefore, the results obtained by applying this criterion are those presented in this work.

CR was evaluated in each cycle (A and B) and for each channel, separately. Figure 9 shows the CR results for each beam and cycle, similarly as it was displayed for LR. In general terms, CR presents an increasing tendency with load level rise. A change in trend is observed when the load

approximately surpasses 50%×P_{max}, where a slope growth increase occurs. The CR variation range was 0 to 0.7.

According to the channels location, a clear grouping of CR response can be noticed. In general, its highest values are in the central channels (C2 and C3), corresponding to the bending span. In particular in those channels of B beams, CR considerably increases from 50%×P_{max} in regard to S beams, for both cycles. This behavior is because cracks occur in the central span earlier and wider than in shear spans and, specifically for B beams, those cracks are the ones that grow up until causing their failure. On the other hand, CR variations between flexural and shear zones are more moderate in S beams, even without such abrupt growth close to the failure. In fact, SP shows almost no zonal differences, meanwhile SF is more tending to incipiently emulate the B beams behavior. AE response in S beams is explained by their failure which is not announced by wide cracks as in B beams, but rather by a pattern of more and thinner cracks throughout their span. Shear cracks also remain more restricted in width until they grow up abruptly at the failure.

In view of the foregoing, CR is linked with cracks width development, rather than with the presence of new cracks as in the case of LR. This also explains why there are higher CR values in B beams (up to 0.7) than in S beams (up to 0.4) since, as is well-known, a higher reinforcement ratio leads to narrower cracks. It should be noted that SF was only evaluated up to 75%×P_{max}, so it is logical to expect higher CR values closer to the failure as occurred in B beams.

It can be also seen in Figure 9 that CR results from cycle A tend to be lower than those calculated in cycle B. There is always scarcer AE activity in repeated loading branch (cycle B) than in the corresponding first loading branch (cycle A). This can be explained because at a repeated cycle, the previous maximum load is not exceeded and, thus, cracks do not propagate as much as in a first cycle after a lower load level. Consequently, the ratio tends to increase for reloading cycles. Also, it can be observed that there are slow initial growth in cycles A -almost flat curves- and a more accelerated growth when exceeding 50%×P_{max}. On the other hand, the tendencies appear to be more linear for cycles B.

Regarding the fibers effect, a very little variations are perceived between BP and BF. In S beams, SF presents slightly higher values than SP after 50%×P_{max}. This would be a direct consequence of the fibers acting as shear reinforcement and leading SF to behave similarly to B beams, since by not failing prematurely it can develop its full crack pattern and subsequently cracks widens in the stabilized stage. In any case, the fibers did not significantly reduce the cracks width (Figure 7 b) and, therefore, an important change in CR due to fibers action is not expected.

A threshold value of CR=0.05 was proposed by [20] in full-scale and more slender RC beams for damage severity classification. This value is in good agreement for limiting the general change in trend observed for CR calculated at cycle A, when the load approximately reached 50%×P_{max}. This observation also supports the fact that the incorporation of fibers did not significantly changes the CR progression tendencies.

Contrary to LR, it is noted that in the last cycle of SP there is not a differentiated CR peak value at C4 where the failure was imminent. This also endorses the conception that this index is linked with cracks width evolution (Figure 9 c and g).

In summary, the results show that the sensors location affects the CR value more than the fibers incorporation, since there are no obvious differences between plain and fiber-reinforced concretes. Moreover, CR gives higher values in reloading cycles than in the first ones.

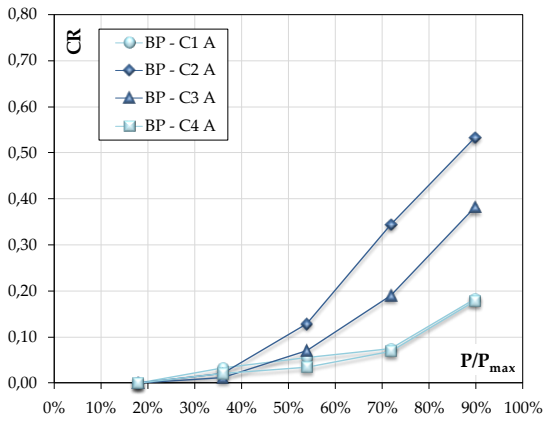
CR
BP - C1 A
BP - C2 A
BP - C3 A
BP - C4 A
P/P max

(a)

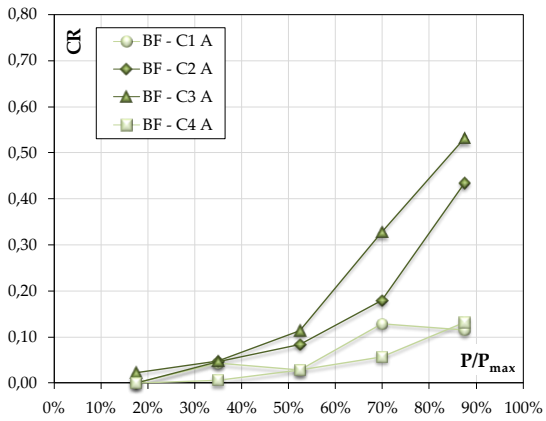
CR
BF - C1 A
BF - C2 A
BF - C3 A
BF - C4 A
P/P max

(b)

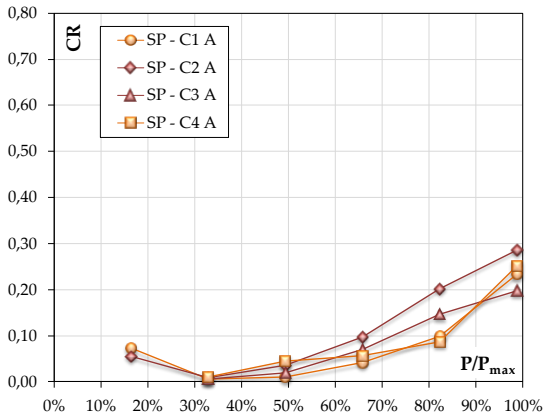
CR
SP - C1 A
SP - C2 A
SP - C3 A
SP - C4 A
P/P max

(c)

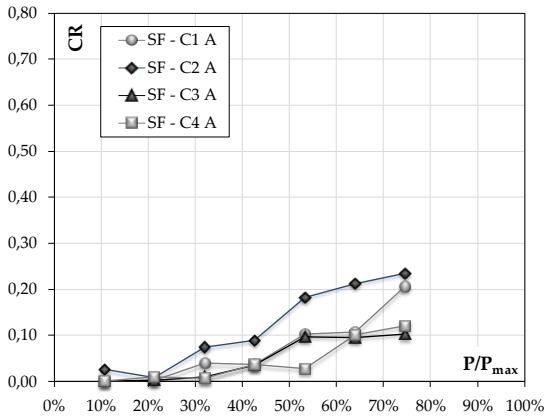
CR
SF - C1 A
SF - C2 A
SF - C3 A
SF - C4 A
P/P max

(d)

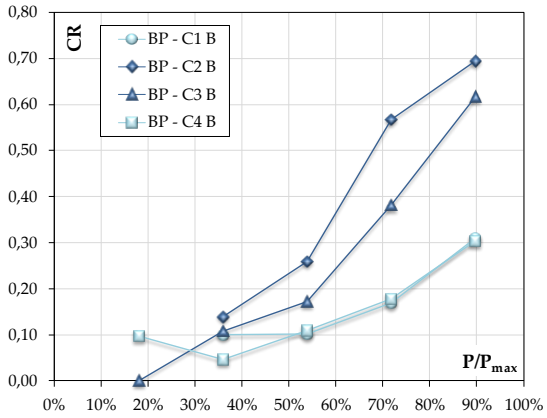
CR
BP - C1 B
BP - C2 B
BP - C3 B
BP - C4 B
P/P max

(e)

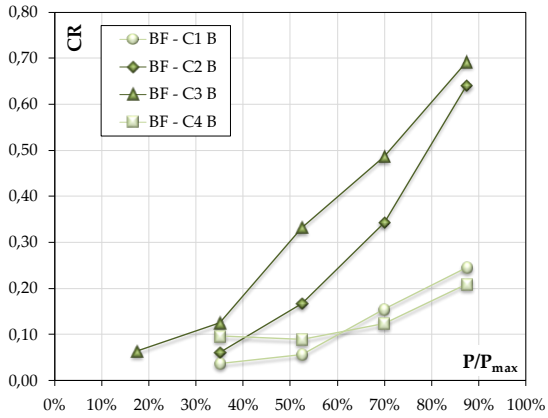
CR
BF - C1 B
BF - C2 B
BF - C3 B
BF - C4 B
P/P max

(f)

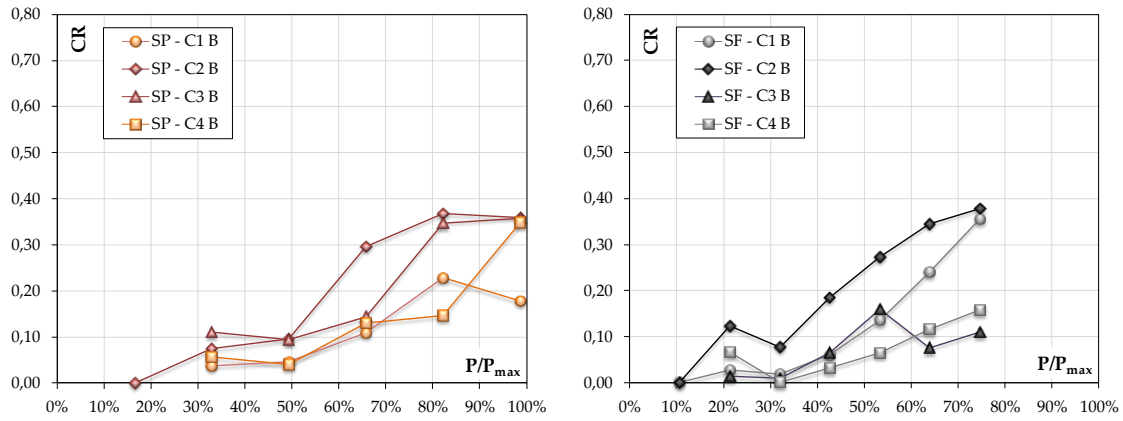

(g) (h)

Figure 9. Calm Ratio results: (a) BP cycle A, (b) BF cycle A, (c) SP cycle A, (d) SF cycle A, (e) BP cycle B, (f) BF cycle B, (g) SP cycle B and (h) SF cycle B.

4.3. Cumulative Signal Strength Ratio (CSSR)

This index was introduced by Ridge and Ziehl [22]. Since it relates the AE in the loading and reloading branches and does not consider the AE in the unloading ones, it has a conceptual similarity to the LR. However, CSSR is not as widespread as the aforementioned indices. By definition, it can only be evaluated when two repetitions at the same load level are performed. Therefore, a single value of CSSR per load level, named A, is presented in this work. It must be pointed out that it has the advantage that is very simple and direct to calculate, without the intrinsic subjectivity of LR.

Figure 10 outlines the CSSR results for each beam, following the previously adopted convention. Meanwhile, Figure 11 presents the CSSR results for all the beams grouped by the AE channels location: (a) those ones in the shear zone and (b) in the flexural zone.

In general, CSSR shows a growing trend when the load level increases, with values mostly ranging between 0 and 0.50. It is observed that zero value is exceeded after the first macrocrack occurs during LL2. This indicates that the Kaiser effect is no longer fulfilled and is equivalent to LR falling below 1.0. In general, CSSR exhibits low dispersion of results, with a relatively symmetric and uniform tendencies. Moreover, as discussed above, the variables analyzed have a little impact on its results.

Regarding the sensors location, it seems not to affect the CSSR at load levels below 50%×P_{max}. In Figure 11, it can be observed that CSSR tends to stabilize horizontally in the flexural span after exceeding 50%×P_{max}, whilst in the shear zones it keeps growing due to the presence of new shear cracks. This suggests that CSSR evolution could be also linked with damage increase and the presence of new macrocracks as LR.

The effect of fibers incorporation is almost imperceptible in the CSSR. BF shows a little lower values than in BP at LL2, demonstrating a more restricted flexural cracks growth. On the other hand, it is observed that SF gives slightly higher values than SP, possibly due to the development of more cracks. It is expected that CSSR values should increase for higher amounts of fibers. Regarding the effect of reinforcement configuration, S beams give lightly higher values than B beams. Again, it would be due to the effect of more of cracks generated by a greater reinforcement ratio. However, these differences are proportionally small.

According to the above, it is appreciated that the CSSR is a clear indicator of cracks presence. In fact, when new cracks appear its value increases and when the existing cracks get stabilized, its value tends to become constant. It is noted that this behavior occurs by zones. As it was mentioned, the beam central zone stabilizes to around 70%×P_{max}, meanwhile the shear zones are

activated closely to the failure. It is noteworthy that, through the CSSR, this internal stresses redistribution from the central span to the supports can be detected in advance from 50%×P_{max}. It can be seen in SP a peak of CSSR = 0.8 at C4 (Figure 10 c), where the failure was impending, likewise as was indicated for LR. The CSSR values in the range of 0 to 0.60, reported by [23] in experiments on smaller and less slender RC beams without fibers, are similar to those obtained here. Thus, the incorporation of fibers did not significantly change the CSSR trends.

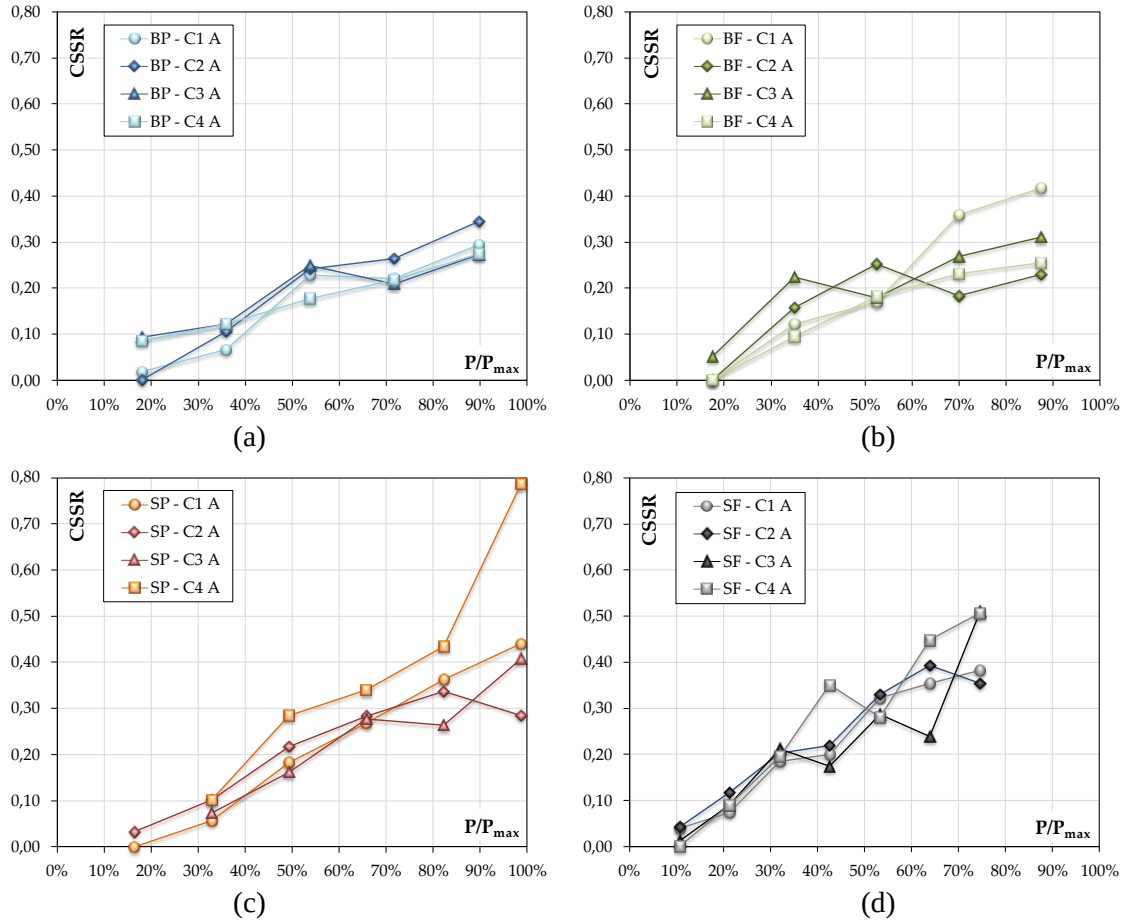

Figure 10. Cumulative Signal Strength Ratio results: (a) BP cycle A, (b) BF cycle A, (c) SP cycle A, (d) SF cycle A.

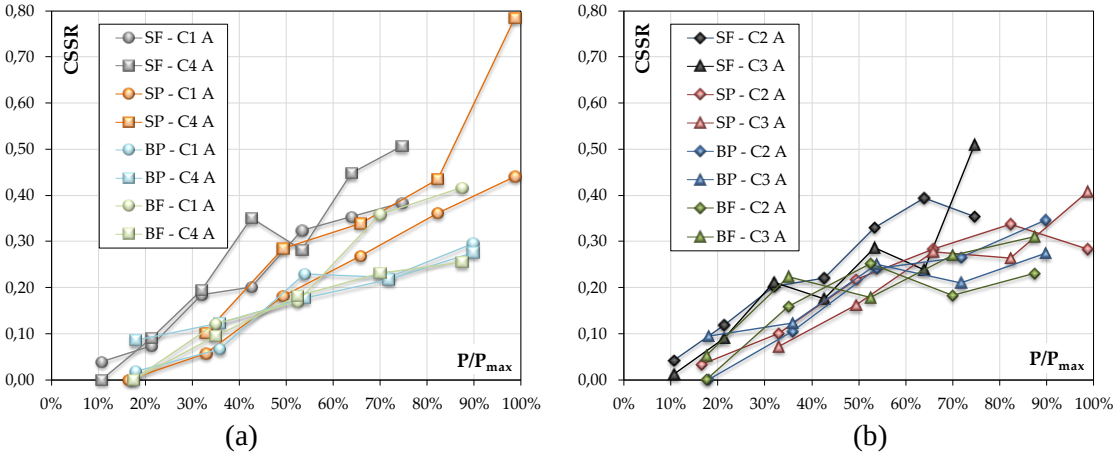

Figure 11. Comparison of Cumulative Signal Strength Ratio results for (a) shear span channels and (b) flexural span channels.

4.4. Relaxation Ratio (RR)

This index, proposed by Colombo et al. [21], is analogous to CR but with some remarkable differences: i) it uses AE Energy as calculation parameter, ii) it is based on average values and iii) the AE activity in the unloading branch is not considered in the ratio denominator. Therefore, RR values can rise above unity. In this work, RR has been adapted. As stated before, AE Signal Strength parameter was considered as a replacement of AE Energy for computations. Moreover, Signal Strength was averaged over the duration of each loading branch.

Figure 12 illustrates RR results for each beam and cycle, equally as the previous indices were displayed. Generally speaking, RR shows an increasing trend with load level. An accelerated rate increase occurs when the load reaches approximately at 50%×P_{max}. RR variation range strongly depends on the analyzed cycle: it ranged from 0 to 1.4 in cycle A, while reached a maximum value of 2.8 in cycle B.

RR response is analogous to CR, its results are also grouped according to sensors location. Higher RR values in the flexural span for all cases can be observed. For B beams, RR values of those channels increase considerably from 60%×P_{max}, in both cycles. In regards to S beams, RR variations between zones are moderate and with lower values than B beams. These behaviors can be explained in the same way as was done for CR. Thus, it suggests that RR is also associated with cracks width evolution, rather than with their formation. In this sense, the wider cracks due to a lower reinforcement ratio explains the higher RR values in B beams (up to 1.4) than in S ones (up to 0.6), at cycle A.

It can be clearly seen that RR, calculated in the first cycle, tends to provide lower numerical results than those in the second cycle. But, unlike CR, the AE activity at unloading branch is not added in the denominator and, thus, its values are prone to be higher. The fibers marginally affects RR behavior. Very limited changes are perceived between BP and BF in cycle A. BP gives slightly higher values than BF in cycle B. For S beams, SF presents a little higher values than SP from 40%×P_{max}, as it was previously mentioned for CR.

A value of RR = 1.0 was exceeded in [21] when 45% ultimate bending load was reached for similar beams size. This value seems to be very high for limiting the damage even for cycle B results, since approximately corresponds to 70-80%×P_{max}.

Summarizing, it was shown that sensors location influences RR values more than the incorporation of fibers, since there are practically no differences between plain and fiber-reinforced specimens. Furthermore, RR results in cycle B are always higher values than in cycle A. Therefore, all the analyzed variables affected RR similarly to CR.

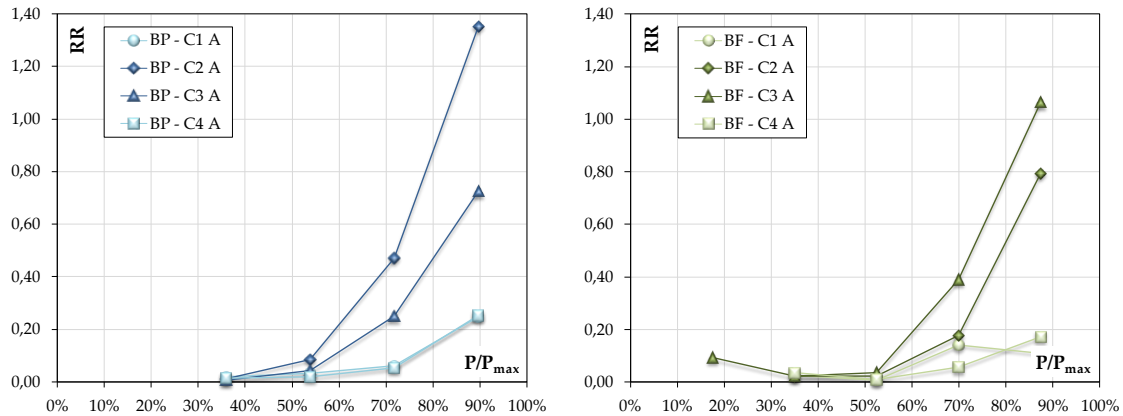

(a) (b)

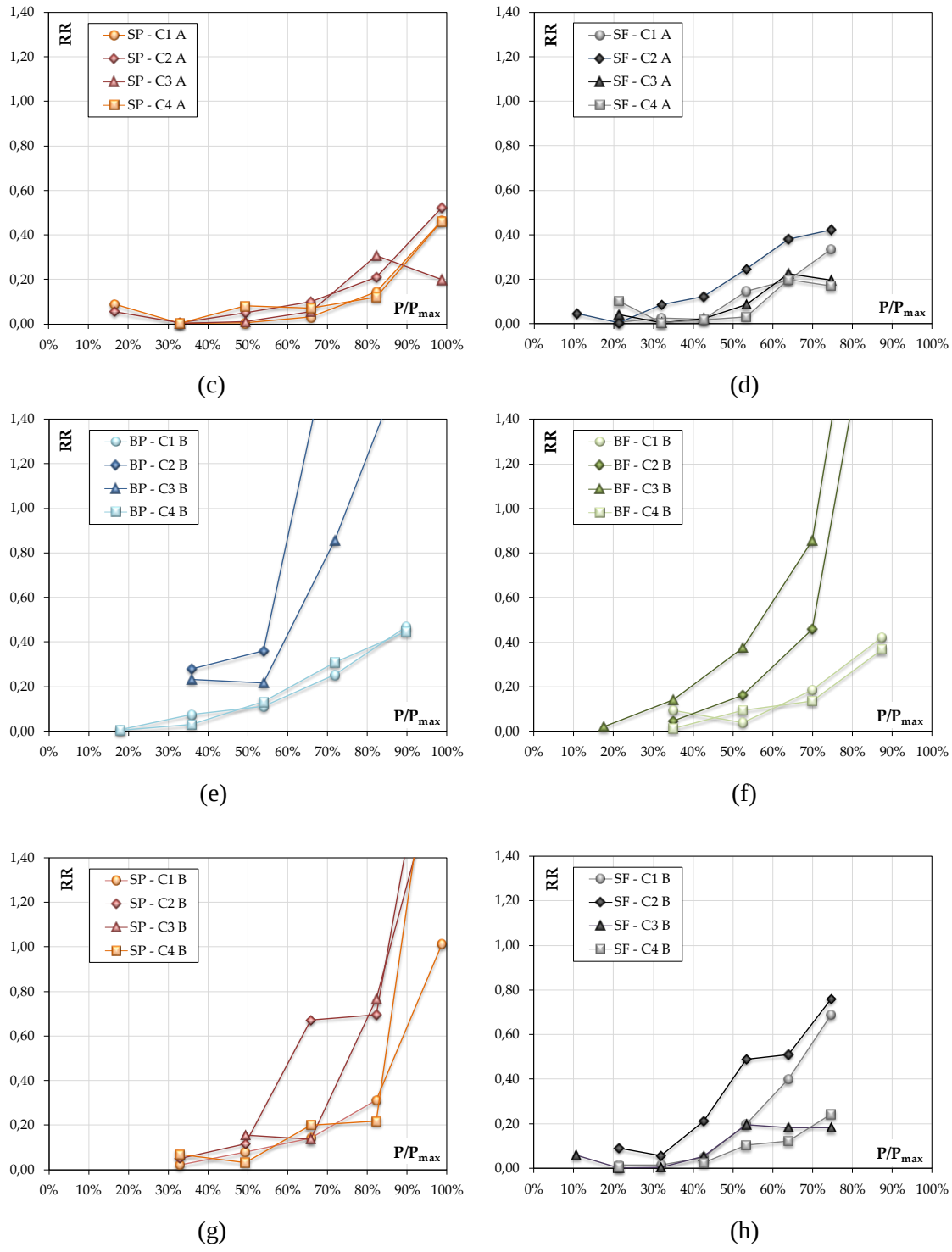

Figure 12. Relaxation Ratio results: (a) BP cycle A, (b) BF cycle A, (c) SP cycle A, (d) SF cycle A, (e) BP cycle B, (f) BF cycle B, (g) SP cycle B and (h) SF cycle B.

4.5. Correlation analysis

After the extensive discussion presented about each AE index, a general remark is highlighted on the symmetry of the tests. Symmetric experimental setup does not necessarily leads to a fully symmetrical structural response. In the RC beams the first cracks appear at maximum stress zone randomly localized where weakness paths exist. As damage increases in a localized area, the

response becomes more asymmetric and an internal redistribution of stresses occurs to balance it. Figure 5 shows that the cracking patterns development is not precisely symmetric as the load increases. Therefore, it is expected that the AE response will not be exactly symmetric either. In general, a certain degree of symmetry in the AE results at Cycle A (between C1 and C2 versus C3 and C4) is observed (Figure 8-to-Figure 12). It is interesting to observe that the curves of the corresponding symmetric channels follow similar trends and seek to match, beyond any numerical offset. As mentioned before, there is always less amount of AE activity in the repeated cycles than in the first ones. As a direct consequence, the ratios can suffer a more significant numerical influence, leading to greater dispersion and loss of global symmetry.

Despite the above remark upon the symmetry, generalized trend lines are proposed to demonstrate the statistical correlations between AE indices and P/P_{max}. In this case, the data set collected from all samples (i.e., BP, BF, SP and SF) were grouped by sensors location (C1-C4 and C2-C3) and reloading cycles (A and B). The scatter plots in Figure 13 actually present the results for the AE indices and their corresponding trend lines (dashed), each one obtained using a set of 46 data points from symmetrically located sensors and including different types of reinforcements.

In general, the relationship between each AE index and P/P_{max} shows a nonlinear tendency, therefore a second-order polynomial trend line ($ax^2 + bx + c$) was chosen. Then, its correlation coefficient R^2 was obtained. Table 5 shows the polynomial trend lines/coefficients (a, b, c) and the corresponding R^2 values. Mostly, the R^2 coefficients show strong correlations (i.e. values greater than 0.7 [43]) between AE indices and the P/P_{max}. It is remarkable that, despite including very diverse cases (i.e., with or without fibers and stirrups) and considering that the AEs and the measurement process by themselves involve very complex physical phenomena, the correlations obtained are considerably good.

The trend lines confirm the characteristics observed and duly discussed in this section for each AE index. Finally, it is important to remark that CSSR and CR provide higher R^2 coefficients than LR and RR, respectively.

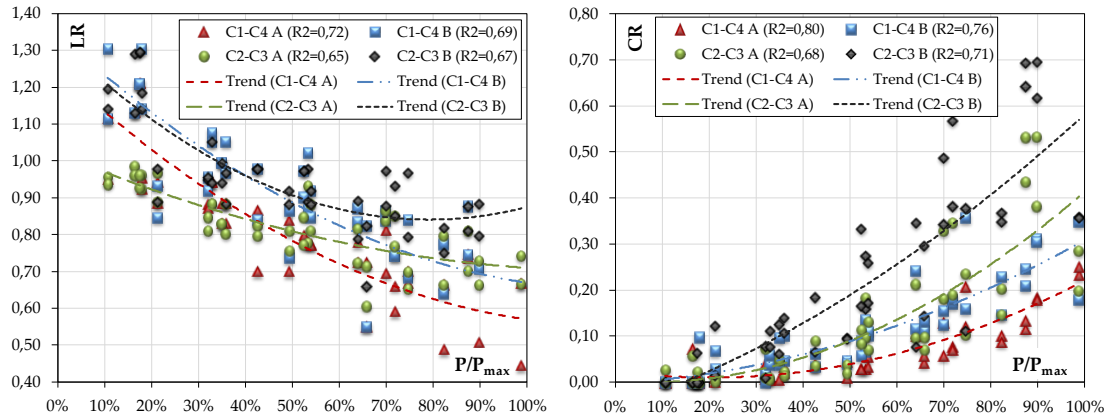

(a) (b)

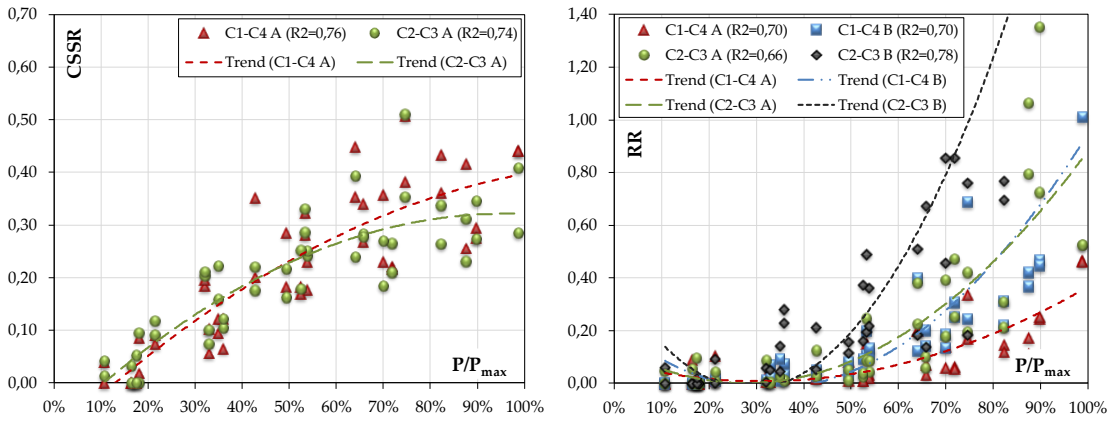

(c) (d)

Figure 13. AE indices plots and trend lines for (a) Load Ratio (b) Calm Ratio (c) Cumulative Signal Strength Ratio and (d) Relaxation Ratio.

Table 5: Quadratic trend lines and correlation coefficients.

Load Ratio				
Trend line	a	b	c	R^2
C1-C4 A	0.50	-1.18	1.25	0.72
C2-C3 A	0.23	-0.54	1.02	0.65
C1-C4 B	0.48	-1.15	1.34	0.69
C2-C3 B	0.78	-1.23	1.33	0.67
Calm Ratio				
Trend line	a	b	c	R^2
C1-C4 A	0.33	-0.14	0.02	0.80
C2-C3 A	0.47	-0.06	0.00	0.68
C1-C4 B	0.26	0.06	0.00	0.76
C2-C3 B	0.29	0.35	-0.06	0.71
Cumulative Signal Strength Ratio				
Trend line	a	b	c	R^2
C1-C4 A	-0.34	0.84	-0.10	0.76
C2-C3 A	-0.44	0.85	-0.08	0.74
Relaxation Ratio				
Trend line	a	b	c	R^2
C1-C4 A	0.75	-0.47	0.08	0.70
C2-C3 A	1.69	-0.94	0.13	0.66
C1-C4 B	2.14	-1.40	0.21	0.70
C2-C3 B	4.81	-2.77	0.38	0.78

4.6. Load Ratio and Calm Ratio chart

Following the proposal of ISO 16837 standard [35], that was addressed at the introductive section, Figure 14 depicts the CR versus LR charts. Besides the convention adopted in the former figures, here the diameter of the spheres are proportional to the P/P_{max} ratio in order to point out the damage level as well.

It can be seen in Figure 14 (a) and (b) that B beams present similar trends. For load levels less than $55\% \times P_{max}$ BP and BF tendencies are almost identical. Afterward, it is perceived that BP has

lower LR values than BF in the shear zones due to a more spread development of inclined cracks. In cycle B the values of both CR and LR increase but, in comparative terms, the behaviors of BP and BF are similar to those described for cycle A.

In Figure 14 (c) and (d) greater differences of S beams behavior can be observed. For service loads under 55%×P_{max}, SP has lower CR values than SF but similar to LR. Then, at higher load levels, SP displays lower LR values than SF in the shear zone. It should be noted that SF was only cycled up to 75%×P_{max}, but their trends indicate that if cycles were continued, CR would had grown approaching B beams. Again, in cycle B, the values of CR and LR tend to increase, but the behaviors of both SP and SF are like those described before for cycle A.

It should be emphasized that the different general aspects between B and S beams charts are misleading due to CR higher values in the flexural span of the B beams and lower LR values in the shear spans of the non-fibered beams, for loads over 55%×P_{max}. However, if the results are limited to 55%×P_{max} and grouped by channels location, as is shown in Figure 15, an interesting coincidence of different beams results can be actually observed. It shows that, for service load levels and crack widths under 0.18 mm, there are not significant differences in the indices values due to the reinforcement configurations. In fact, the results seem to be more affected by sensors location and in which cycle repetition the indices are calculated. Moreover, this fact allows to setup global limit values.

Based on the results, reference values to limit the damage at 55%×P_{max} would be CR = 0.05 and LR = 0.75 for the first loading cycles (A) and LR = 0.85 for subsequent repeated loading cycles.

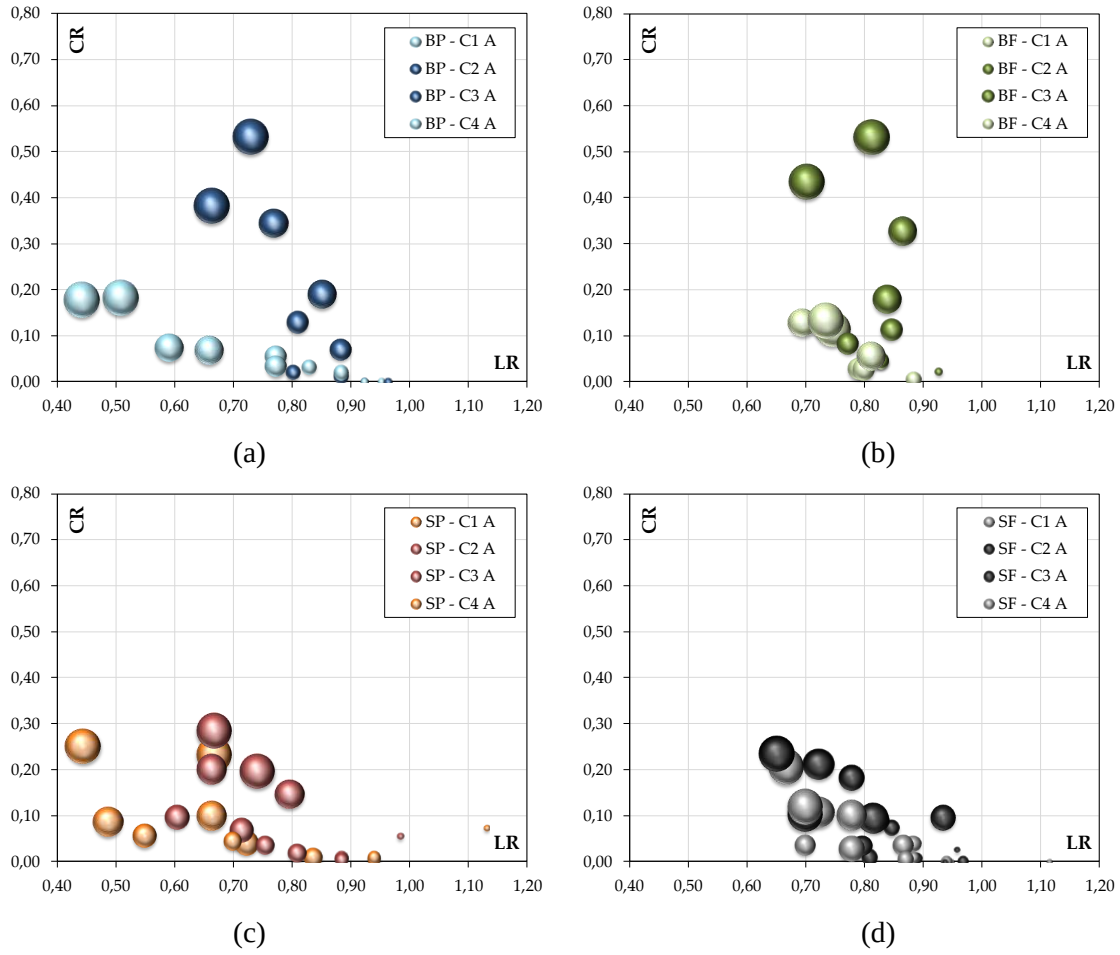

(a) (b)

(c) (d)

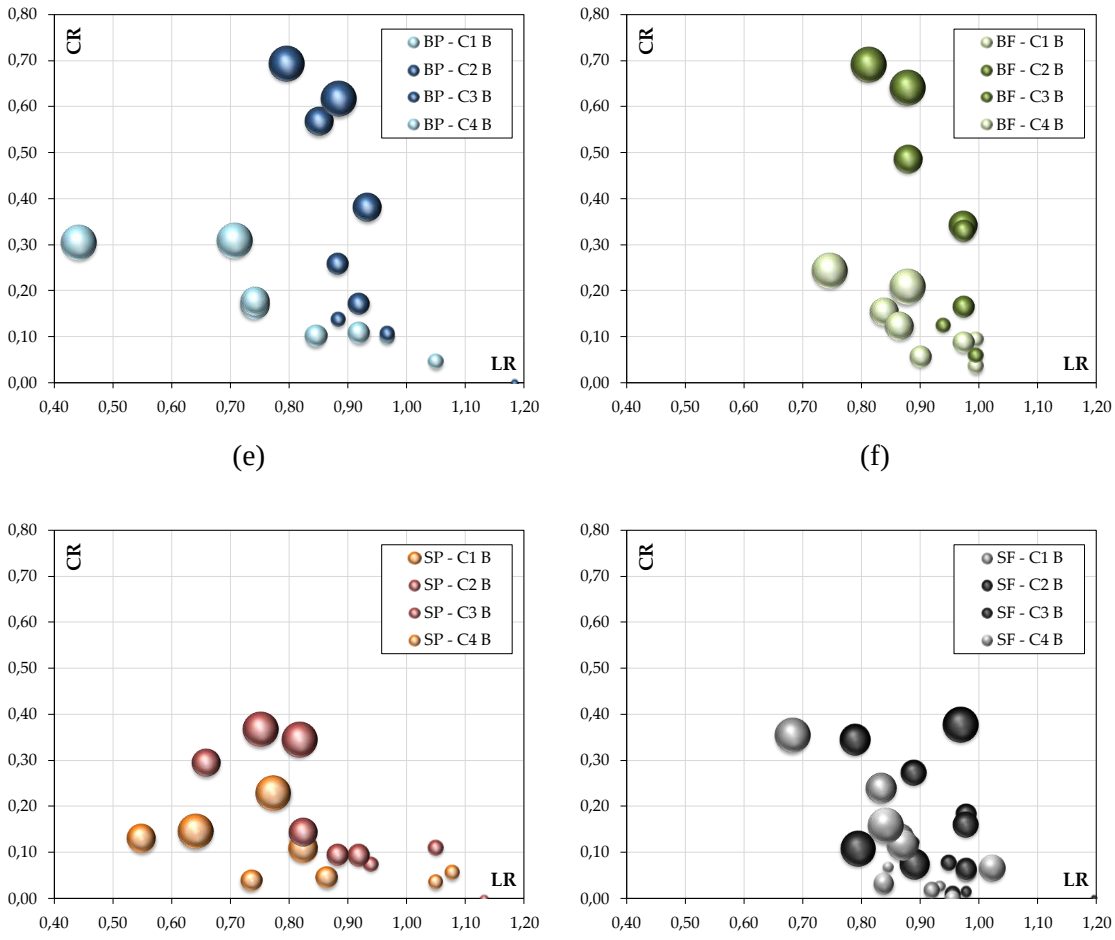

Figure 14. Load Ratio vs. Calm Ratio charts (a) BP cycle A, (b) BF cycle A, (c) SP cycle A, (d) SF cycle A, (e) BP cycle B, (f) BF cycle B, (g) SP cycle B and (h) SF cycle B.

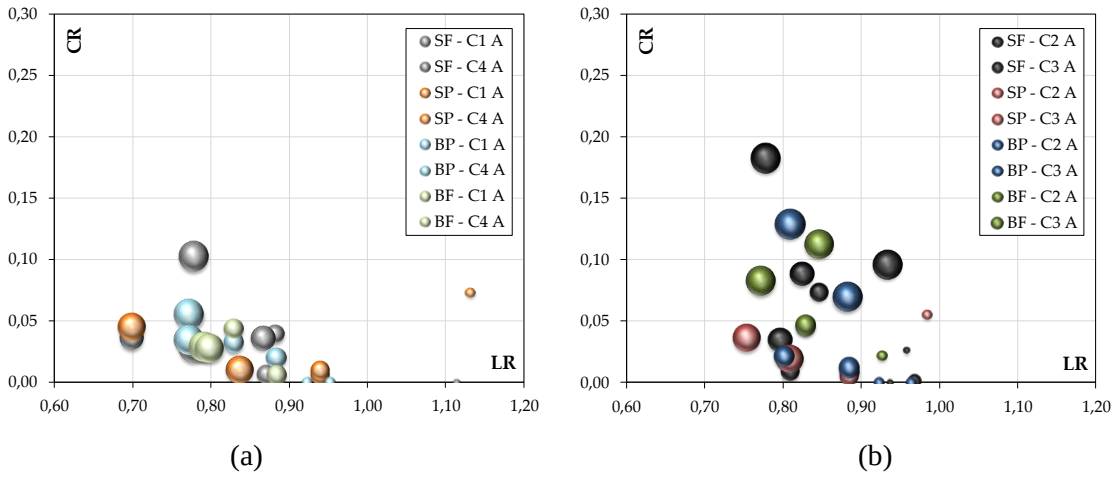

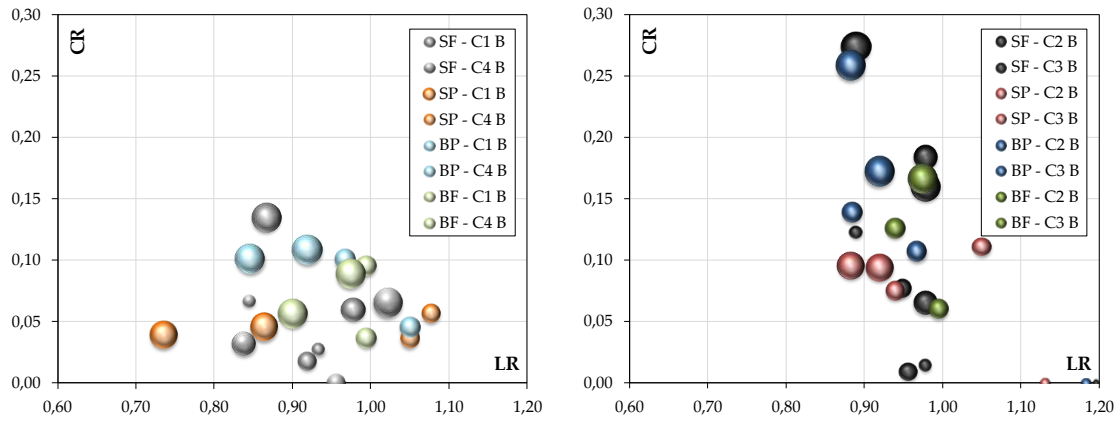

Figure 15. Load Ratio vs. Calm Ratio charts limited to 55%×P_{max} (a) shear span channels at cycle A, (b) flexural span channels at cycle A, (c) shear span channels at cycle B and (d) flexural span channels at cycle B.

5 CONCLUSIONS

In this work, structural and AE test results on RC beams, with and without steel fibers and loaded in cycles up to failure, were presented. The analysis of the AE data was based on the following four indices proposed in the scientific literature: Load Ratio (LR), Calm Ratio (CR), Cumulative Signal Strength Ratio (CSSR) and Relaxation Ratio (RR).

Although ISO 16837 standard is an important step forward for implementing a AE-based damage assessment in RC beams, there is still a lack of clear understanding about the applicability boundaries of the analyzed AE indices. Specifically, how certain key variables, (e.g., sensors location, reinforcement configurations and cyclic loading procedure), affect its results and therefore, their limit values for damage qualification. This work was aimed at providing experimental evidence when steel fibers are incorporated into concrete mixture and also on the effect of the aforementioned variables on the results of the selected AE indices.

The following conclusions can be drawn based on the experimental campaign:

- The addition of steel fibers modified the structural behavior of the RC beam without stirrups by improving shear strength. Specifically, its failure shifted from a premature shear mode to bending-like one, by arresting inclined cracks growth. Hence, in terms of AE activity, fibers lead to behave as a bending type response.
- Fibers bridging mechanisms acted at restricting initial crack developments, for low load levels (LL2). However, due to the moderate adopted volume fraction of 0.5% of steel fibers, this effect was very limited.
- AE indices results showed a quite good correlation with P/P_{max}, the latter chosen as a damage parameter. Although, in previous works of the literature, differentiated AE behaviors have been reported for shear and bending failures, in this work, the LR and CR trends (for both B and S samples) were not so different at service load levels when represented in terms of P/P_{max}. Therefore, it makes possible to integrate them in a global damage criterion, regardless of the reinforcement configurations and amounts. This finding is auspicious for its application in load tests as a complementary and non-destructive tool for detecting and limiting excessive damage generation.
- A great influence on the AE results was appreciated by sensors location in relation to the stresses zones. This must be carefully taken into account when instrumenting a structural element so as to avoid losing crucial data for damage assessment. Consequently, the

stresses distribution throughout the structural element must be estimated in advance as faithfully as possible.

- The loading procedure and its cycle repetitions strongly affected AE indices results. As stated above, the experimental beams were new, never loaded before and uncracked. Nevertheless, it is supposed that it could lead at revealing the historical maximum applied load level by just comparing the indices variation between consecutive identical cycles. Thus, it is recommended to perform at least two twin cycles per load level. Certainly, more researches must be done to verify this presumption. Also, it is recommended to carry out tests by considering several load levels, i.e., small load incremental steps, in order to obtain reliable trends. Otherwise, a damage assessment misinterpretation by means of the lack of intermediate evaluation points can occur.
- CSSR led to stable and uniform trends and, hence, suggests to be an alternative for the LR, as its evaluation is not subjective. Both indices seem to be related to the same physical phenomena: presence and severity of new cracks and damage evolution.
- RR presented similar tendencies to CR but increased with higher rates. Both indices appear to be strongly related to the cracks width growth. On the one hand, RR has the advantage that it can contemplate different duration of the loading/unloading phases at the same cycle. But as a disadvantage, greater dispersions of the results can be observed for RR than CR. In the light of the foregoing, RR could be convenient as a possible replacement to CR for "in situ" testing, because in those cases is more difficult to obtain a constant loading rate.
- The results in this work confirm the convenience of linking two complementary AE indices (e.g., LR or CSSR and CR or RR) for assessing damage states since they focus on different aspects of the cracking progress.

Further studies are necessary and will be oriented on improving testing procedures with AE and on identifying limit states for RC beams, at different exposure conditions, through AE evaluation.

Furthermore, a proposal linking AE indices and cracking/failure modes at different levels of observation is currently under development. In this regard, analyses and discussions are being carried out at material scale (i.e., micro and meso-scales) considering RA value vs AF (Average Frequency) and at macro-to-structural scale considering global AE indices.

Acknowledgements

The authors would like to thank the valuable assistance of Eng. Nicolás Rocca, Eng. Luciano Sambataro, Eng. Adrián Comelli at performing the experimental campaign. The contribution of technical staff of the Laboratory of Materials and Structures of the University of Buenos Aires (UBA) is also gratefully acknowledged, specially to Mr. Franco Dios, Eng. Marcelo Net and Eng. Gregorio Pytlowany. Finally, the first author also would like to thank Dr. Martín Gómez for his valuable discussions.

References

1. Aseem, A., Baloch, W. L., Khushnood, R. A., & Mushtaq, A. (2019). Structural health assessment of fire damaged building using non-destructive testing and micro-graphical forensic analysis: A case study. Case Studies in Construction Materials, 11, e00258.
2. Liao, S. T., Tong, J. H., Chen, C. H., & Wu, T. T. (2006). Numerical simulation and experimental study of parallel seismic test for piles. International Journal of Solids and Structures, 43(7-8), 2279-2298.
3. Davis, A. G., Lim, M. K., & Petersen, C. G. (2005). Rapid and economical evaluation of concrete tunnel linings with impulse response and impulse radar non-destructive methods. NDT & E International, 38(3), 181-186.

4. Nowotarski, P., Dubas, S., & Milwicz, R. (2017). Review of the Air-Coupled Impact-Echo Method for Non-Destructive Testing. In IOP Conference Series: Materials Science and Engineering (Vol. 245, No. 3, p. 032098). IOP Publishing.
5. Menningen, J., Siegesmund, S., Tweeton, D., & Träupmann, M. (2018). Ultrasonic tomography: non-destructive evaluation of the weathering state on a marble obelisk, considering the effects of structural properties. Environmental Earth Sciences, 77(17), 601.
6. Tosti, F., Ciampoli, L. B., D'Amico, F., Alani, A. M., & Benedetto, A. (2018). An experimental-based model for the assessment of the mechanical properties of road pavements using ground-penetrating radar. Construction and Building Materials, 165, 966-974.
7. Brazee, N. J., Marra, R. E., Göcke, L., & Van Wassenaer, P. (2011). Non-destructive assessment of internal decay in three hardwood species of northeastern North America using sonic and electrical impedance tomography. Forestry, 84(1), 33-39.
8. Behnia, A., Chai, H. K., & Shiotani, T. (2014). Advanced structural health monitoring of concrete structures with the aid of acoustic emission. Construction and Building Materials, 65, 282-302.
9. Omondi, B., Aggelis, D. G., Sol, H., & Sitters, C. (2016). Improved crack monitoring in structural concrete by combined acoustic emission and digital image correlation techniques. Structural Health Monitoring, 15(3), 359-378.
10. Lacidogna, G., Piana, G., & Carpinteri, A. (2019). Damage monitoring of three-point bending concrete specimens by acoustic emission and resonant frequency analysis. Engineering Fracture Mechanics, 210, 203-211.
11. Lacidogna, G., Piana, G., Accornero, F., & Carpinteri, A. (2020). Multi-technique damage monitoring of concrete beams: Acoustic Emission, Digital Image Correlation, Dynamic Identification. Construction and Building Materials, 242, 118114.
12. ASTM E 1316, 2004, Standard Terminology for Nondestructive Testing, Books of Standards, ASTM International, W. Conshohocken, Pennsylvania, USA, 40 pp.
13. Grosse, C.U. and Ohtsu, M., Acoustic Emission Testing, Springer-Verlag, Heidelberg, 2008.
14. Carnì, D.L., Scuro, C., Lamonaca, F., Olivito, R.S., & Grimaldi, D. (2017). Damage analysis of concrete structures by means of acoustic emissions technique. Composites Part B 115: 79-86.
15. Carpinteri, A., Lacidogna, G., Accornero, F., Mpalaskas, A.C, Matikas, T.E. & Aggelis, D.G. (2013). Influence of damage in the acoustic emission parameters. Cement & Concrete Composites 44: 9-16.
16. Colombo, S., Main, I.G., & Forde, M.C. (2003). Assessing damage of reinforced concrete beam using "b-value" analysis of acoustic emission signals. J. Mater. Civil Eng. ASCE 15:280-6.
17. Prem, P.R. and Murthy, A. R. (2017). Acoustic emission monitoring of reinforced concrete beams subjected to four-point-bending. Applied Acoustics 117: 28-38.
18. Schumacher, T., Higgins, C. C., & Lovejoy, S. C. (2011). Estimating operating load conditions on reinforced concrete highway bridges with b-value analysis from acoustic emission monitoring. Struc. Health Monitor. 10(1): 17-32.
19. Golaski, L., Gebski, P. & Ono, K. (2002). Diagnostics of reinforced concrete bridges by acoustic emission. J. Acoustic Emission 20: 83-9.
20. Ohtsu, M., Uchida, M., Okamoto, T. & Yuyama, S. (2002). Damage Assessment of Reinforced Concrete Beams Qualified by Acoustic Emission. ACI Structural Journal, 99(4): 411-417.
21. Colombo, S., Forde, M.C., Main, I.G. & Shigeishi, M. (2005). Predicting the ultimate bending capacity of concrete beams from the "relaxation ratio" analysis of AE signals. Construction and Building Materials, 19, 746-754.
22. Ridge, A., and Ziehl, P. (2006). Evaluation of Strengthened Reinforced Concrete Beams: Cyclic Load Test and Acoustic Emission Methods," ACI Structural Journal, 103(6): 832-841.
23. Liu, Z., and Ziehl, P. (2009). Evaluation of reinforced concrete beam specimens with acoustic emission and cyclic load test methods. ACI Structural Journal, 106(3): 288-299.
24. Vidya Sagar, R., Raghu Prasad, B.K. & Singh, R.K. (2015). Kaiser effect observation in reinforced concrete structures and its use for damage assessment, Archives of Civil and Mechanical Engineering, 548-557.
25. Jiang, Y. D., Xian, X. F., & Xu, J. (2005). Research on application of Kaiser effect of acoustic emission to measuring initial stress in rock mass. ROCK AND SOIL MECHANICS-WUHAN, 26(6), 946.
26. Mabry, N., Banks, C., Toutanji, H. & Seif, M. (2011). Acoustic emission felicity ratio measurements in carbon composites laminates using fiber Bragg grating sensors. In Smart Sensor Phenomena, Technology, Networks, and Systems 2011 (Vol. 7982, p. 79820Y). International Society for Optics and Photonics.

27. Lei, X., Funatsu, T., Ma, S., & Liu, L. (2016). A laboratory acoustic emission experiment and numerical simulation of rock fracture driven by a high-pressure fluid source. Journal of Rock Mechanics and Geotechnical Engineering, 8(1), 27-34.
28. Landis, E. N. (1999). Micro–macro fracture relationships and acoustic emissions in concrete. Construction and Building Materials, 13(1-2), 65-72.
29. Iturrioz, I., Birck, G., & Riera, J. D. (2019). Numerical DEM simulation of the evolution of damage and AE preceding failure of structural components. Engineering Fracture Mechanics, 210, 247-256.
30. Kocur, G. K., Saenger, E. H., Grosse, C. U., & Vogel, T. (2016). Time reverse modeling of acoustic emissions in a reinforced concrete beam. Ultrasonics, 65, 96-104.
31. Saenger, E. H., Kocur, G. K., Jud, R., & Torrilhon, M. (2011). Application of time reverse modeling on ultrasonic non-destructive testing of concrete. Applied Mathematical Modelling, 35(2), 807-816.
32. Xiao, F., & Liu, G. (2014). Test of Acoustic Emission Characteristic and COMSOL Simulation of Coal-body Failure in Methane Drainage Bore-hole under Complex Stress. Electronic Journal of Geotechnical Engineering. 19, 2367-2378.
33. Zou, Q. Y., & Dong, X. C. (2012). Finite element simulation of crack testing system of electromagnetic acoustic emission based on ANSYS. In Advanced Materials Research (Vol. 424, pp. 1097-1101). Trans Tech Publications Ltd.
34. Chiappa, A., Giorgetti, F., Marzani, A., Messina, M., Augugliaro, G., Mennuti, C., & Biancolini, M. E. (2018). Comparison of numerical models for Acoustic Emission propagation. Procedia Structural Integrity, 12, 353-369.
35. ISO 16837, 2019, Non-destructive testing - Acoustic emission testing - Test method for damage qualification of reinforced concrete beams, International Organization for Standardization, Geneva, Switzerland, 5 pp.
36. RILEM TC 212-ACD, 2010, Acoustic emission and related NDE techniques for crack detection and damage evaluation in concrete. Test method for damage qualification of reinforced concrete beams by acoustic emission, Materials and Structures, 43, 1183-1186.
37. NDIS 2421, 2000, Recommended practice for in situ monitoring of concrete structures by AE, Japanese Society for Nondestructive Inspection (JSNDI), Tokyo, Japan, 6 pp.
38. Aggelis, D., Soulioti, D., Sapouridis, N., Barkoula, N., Paipetis, A. & Matikas T. (2011). Acoustic emission characterization of the fracture process in fibre reinforced concrete. Construction and Building Materials, 25(11): 4126-4131.
39. Xargay, H., Folino, P., Nuñez, N., Gómez, M., Caggiano, A. & Martinelli, E. (2018). Acoustic Emission behavior of thermally damaged Self-Compacting High Strength Fiber Reinforced Concrete. Construction and Building Materials, 187, 519-530.
40. Ozawa, M., Uchida, S., Kamada, T. & Morimoto, H. (2012). Study of mechanisms of explosive spalling in high-strength concrete at high temperatures using acoustic emission. Construction and Building Materials, 37: 621-628.
41. Folino, P., Ripani, M., Xargay, H., & Rocca, N. (2020). Comprehensive analysis of Fiber Reinforced Concrete beams with conventional reinforcement. Engineering Structures, 202, 109862.
42. ACI 437.2M-13, 2013, Code requirements for Load Testing of Existing Concrete Structures and Commentary. ACI Committee 437, American Concrete Institute, Farmington Hills, MI, USA, 25 pp.
43. Moore, D. S., Notz, W., & Fligner, M. A. (2013). The basic practice of statistics. 774pp.